RSC Advances

PAPER

View Article Online
View Journal | View Issue

Cite this: *RSC Adv.*, 2025, **15**, 43983

Sustainable zeolite/activated carbon nanocomposite for dual-dye adsorption, kinetic and thermodynamic studies, and urea electro-oxidation applications

Abdullah S. Alawam,[a] Samar M. Mahgoub,[b] Ahmed A. Allam,[a] Abdelatty M. Radalla,[c] Marwa H. Shemy[c] and Rehab Mahmoud *[c]

This study developed a novel zeolite/activated carbon nanocomposite (Zeo/AC) for the simultaneous removal of carcinogenic Congo Red (CR) and Crystal Violet (CV) dyes, with subsequent energy recovery. The material was synthesized *via* a green ball milling-hydrothermal method and characterized thoroughly. The Zeo/AC nanocomposite demonstrated exceptional adsorption performance, achieving record capacities of 752.6 mg g^{-1} for CR and 908.3 mg g^{-1} for CV at 55 °C and neutral pH. Adsorption was rapid, reaching equilibrium within 60 minutes and following pseudo-second-order kinetics (R^2 > 0.998). The process was endothermic and spontaneous. The intermediate pHpzc (6.1) enabled efficient dual-dye removal *via* synergistic mechanisms: electrostatic attraction for cationic CV and π–π stacking/pore filling for anionic CR. Statistical physics modeling confirmed physisorption-dominated interactions ($\Delta E \approx -12$ kJ mol^{-1}). The composite exhibited excellent regenerability, retaining >82% capacity over five cycles. As a proof-of-concept for a circular economy, the dye-saturated adsorbent was successfully repurposed as an electrode for urea electro-oxidation, delivering a current density of 15.45 mA cm^{-2}. The synthesis method and application were validated as environmentally friendly by greenness assessment tools (AGREEprep, BAGI, RGB12). This work presents a sustainable, dual-function material for advanced wastewater treatment and resource valorization.

Received 1st September 2025
Accepted 31st October 2025

DOI: 10.1039/d5ra06559c

rsc.li/rsc-advances

1 Introduction

The growing environmental impact of the textile industry is exemplified by its ongoing expansion, with annual production reaching about 700 000 tons of synthetic dyes, around 60–70% of which consist of azo dyes.[1,2] Large volumes of wastewater containing azo dyes are discharged into aquatic ecosystem.[3] Among azo dyes, Congo red (CR) and crystal violet (CV) represent two of the most problematic synthetic dyes due to their extensive industrial application.[3]

These dyes are favored in the textile, printing, and biological staining industries owing to their excellent color fastness, stability, and affinity for various substrates. However, these very properties that make them commercially valuable also contribute to their persistence and hazardous nature in the environment.

Beyond their direct toxic effects, both Congo red and crystal violet pose significant metabolic risks. Congo red, as a benzidine-based azo dye, can undergo metabolic reduction by intestinal and environmental microorganisms, leading to the formation of carcinogenic aromatic amines including benzidine. These metabolic products are known human carcinogens that can interact with DNA and cause mutagenic effects[4] Similarly, crystal violet can be metabolically transformed into leucocrystal violet and other derivatives through reduction processes, which exhibit different toxicological profiles and enhanced bioaccumulation potential. The metabolic transformation of these dyes in both biological systems and environmental compartments significantly influences their overall toxicity, persistence, and ecological impact, making understanding these pathways crucial for comprehensive risk assessment[5,6]

Congo red dye, a benzidine-based azo dye ($C_{32}H_{22}N_6Na_2O_6S_2$), continues to be a persistent pollutant of environmental concern. CR being one of the 80% of industrially used and discharged dyes, ultimately producing toxic nature.[3] The discharge of CR into water sources by factories has been

[a]*Department of Biology, College of Science, Imam Mohammad Ibn Saud Islamic University (IMSIU), Riyadh 11623, Saudi Arabia. E-mail: asalawam@imamu.edu.sa; aallam@imamu.edu.sa*

[b]*Materials Science and Nanotechnology Department, Faculty of Postgraduate Studies for Advanced Sciences, Beni-Suef University, Beni-Suef 62511, Egypt. E-mail: miramar15@yahoo.com*

[c]*Chemistry Department, Faculty of Science, Beni-Suef University, Beni-Suef 62511, Egypt. E-mail: rehabkhaled@science.bsu.edu.eg; abdelaty.mohamed@science.bsu.edu.eg; marwa.h.shemy@gmail.com*

associated with a range of health concerns, such as cancer, redness, skin irritation, allergic reactions, and mutagenic effects from its metabolic breakdown products.[7,8] Additionally, the bioaccumulation of CR in aquatic organisms is a critical concern, negatively impacting their survival and reproductive capabilities.[3] Similarly, crystal violet, a triphenylmethane dye ($C_{25}H_{30}ClN_3$), poses equally severe environmental threats. Its non-biodegradable nature and tendency to form stable complexes with organic matter result in prolonged environmental persistence.[9] The dye exhibits toxicity toward fish, causing gill damage, liver dysfunction, and reproductive disorders.[10] Even at low concentrations (as little as 1 mg L^{-1}), the high color intensity of both dyes blocks light penetration in water, which hinders the photosynthetic activity that supports the ecosystem's productivity.

To quantitatively assess these risks, the threshold concentrations at which Congo red (CR) and Crystal violet (CV) become environmentally hazardous are well-established in ecotoxicological literature. CR exhibits a 48-hour EC_{50} of 17.0 mg L^{-1} and LC_{50} of 322.9 mg L^{-1} in *Daphnia magna*, with bacterial growth inhibition occurring above 300 mg L^{-1}, indicating significant toxicity at these levels.[11] In contrast, CV is toxic at much lower concentrations, with a 48-hour EC_{50} of 75.9 μg L^{-1} and LC_{50} of 629.4 μg L^{-1} in *Daphnia pulex*, and adverse effects observed in humans and animals even at 1 μg L^{-1}, confirming its high potency. These values demonstrate that while both dyes are not pollutants at all concentrations, they pose substantial ecological and health risks beyond these thresholds, justifying their classification as environmental contaminants.

Given that CR and CV are so persistent and resist traditional biological treatments, the development of advanced remediation technologies is crucial.[12]

A variety of methods have been investigated for the removal of CR and CV from aqueous solutions. These approaches include coagulation–flocculation, biological treatment, adsorption, chemical oxidation, membrane filtration, and advanced oxidation processes (AOPs). Among these, electrochemical advanced oxidation processes (EAOPs) have emerged as particularly promising due to their high efficiency in degrading recalcitrant organic pollutants like dyes, without generating secondary waste streams. The electrochemical mineralization of azo and triphenylmethane dyes can achieve complete degradation through direct electron transfer or indirect oxidation *via* generated hydroxyl radicals, making these techniques especially suitable for treating persistent dyes like CR and CV.[13] Biological treatment methods have shown limited efficacy for dye removal due to the xenobiotic nature of synthetic dyes, which makes them difficult for microorganisms to degrade. For instance, conventional activated sludge processes typically achieve less than 20% removal of both CR and CV because these dyes inhibit microbial communities.[14] Chemical oxidation processes, including ozonation and Fenton oxidation, have demonstrated moderate success. Using a Fenton process, for example, studies have reported effective removal of CR and CV. However, this method is limited by a combination of factors, including its high chemical and energy consumption, the significant number of residues it generates, and its overall lack of environmental sustainability, which ultimately restricts its practical application.[15–17] Although UV light-assisted photodegradation and membrane technologies have shown high removal efficiencies while membrane processes are hindered by fouling, high costs, and difficulties in disposing of the concentrated waste dye.[17–20]

Among all these methods, adsorption is the most promising and widely common method for removing dyes due to its advantages. It is simple, cost-effective, highly efficient, sustainable, and flexible. Unlike other methods, adsorption is environmentally friendly due to working under mild conditions, needing minimal chemical additives, and avoiding toxic by-products.[16] Adsorption has the ability to regenerate adsorbents, which allows for over 90% removal efficiency of various synthetic dyes. The adsorption process is influenced by various factors, but the adsorbent material is the one that has garnered the most attention in recent research. The selection of an appropriate adsorbent is based on several properties, such as its effectiveness, safety, cost, availability, sustainability, reusability, biodegradability, and durability.[17]

In recent decades, many natural and synthetic adsorbents have been used for the removal of CR and CV including zeolites, biomass wastes, fly ash, algae, activated carbon, nanocomposites, biobased materials, nanoparticles, and synthetic polymers because of their availability, adsorption capacity, and reusability.[18] Among the used adsorbents, zeolites are promising natural adsorbents for dye removal, because of their large surface area, high cation exchange capacity, and natural abundance.

Within the zeolite family, clinoptilolite, a porous aluminosilicates $(Na_2K_2CaMg)_3[AlO_2]_6[SiO_2]_{30}\cdot 24H_2O$ is commonly one of forms due to its high surface area, porosity, adsorption capacity, eco-friendly nature, and excellent thermal and mechanical durability further enhance its appeal as a dye removal adsorbent.[19–21] As reported, modification of clinoptilolite plays a crucial role in enhancing its surface activity, ion-exchange capacity, catalytic potential, and adsorption performance to remove CR and CV.[22]

Modified zeolites are enhanced forms of natural or synthetic zeolites that undergo chemical, physical, or structural alterations to improve their performance. Through methods such as ion exchange, surface functionalization, nanoparticle doping, or compositing with carbon, their surface area, pore structure, and active sites are optimized.[23] These modifications significantly boost adsorption capacity, catalytic activity, and selectivity, making them highly efficient for removing heavy metals, dyes, and organic pollutants. Thus, modified zeolites serve as versatile and sustainable materials for advanced water treatment applications. Modified zeolites are enhanced forms of natural or synthetic zeolites that undergo ion exchange, surface functionalization, nanoparticle doping, or compositing with carbon, their surface area, pore structure, and active sites are optimized.[24,25] These modifications significantly boost adsorption capacity, catalytic activity, and selectivity, making them highly efficient for removing, dyes, and organic pollutants. Modified clinoptilolite is crucial for improving its performance in removing Congo red (CR) and crystal violet (CV) dyes.[22,23]

Activated carbon remains the gold standard for adsorption applications due to its extremely high surface area (500–1500 m^2 g^{-1}) and well-developed pore structure. Activated carbon prepared from coffee waste as an adsorbent for the removal of Congo red dye from aqueous solution showed that oxygen-containing groups play an important role in dye adsorption.[26]

Zeolites and activated carbon represent two of the most promising adsorbent materials for dye removal applications. Their unique structural properties and high surface areas make them exceptionally effective for adsorption processes. The combination of zeolites and activated carbon creates synergistic effects that enhance overall adsorption performance.[27] This enhancement results from complementary adsorption mechanisms: zeolites provide ion exchange sites and uniform micropores, while activated carbon contributes high surface area and diverse pore size.

The field of sustainability is moving beyond traditional waste management, shifting from using simple adsorbents to a more productive, circular model. Rather than merely treating pollutants and then disposing of the saturated material, this new approach re-envisions adsorbents as a valuable resource. Affordability, longevity, and efficiency make Direct Urea Fuel Cells (DUFCs) a compelling option for sustainable, portable power. These cells can harness energy from a variety of fuels, including renewable ones.[28] Efforts to enhance urea oxidation have led to the exploration of non-platinum catalysts. Among these, carbon-based electrocatalysts present a compelling alternative due to their excellent conductivity, larger active surface area, and lower cost.[29]

This study addresses these critical research gaps through three key innovations: first, we developed a novel zeolite-activated carbon (Zeo/AC) nanocomposite specifically engineered for simultaneous removal of both anionic CR and cationic CV dyes, achieving unprecedented adsorption capacities of 752.6 mg g^{-1} for CR and 908.3 mg g^{-1} for CV under neutral pH conditions. Second, we demonstrate a circular economy approach by repurposing the spent dye-loaded adsorbent as an effective electrocatalyst for urea electrooxidation in direct urea fuel cells, achieving current densities of 15.45 mA cm^{-2}. Third, we provide comprehensive mechanistic insights through complementary classical thermodynamics and statistical physics modeling, elucidating both macroscopic and molecular-level adsorption mechanisms. The sustainable synthesis was validated using multiple greenness assessment tools (AGREEprep, BAGI, RGB12), confirming the environmental compatibility of our approach.

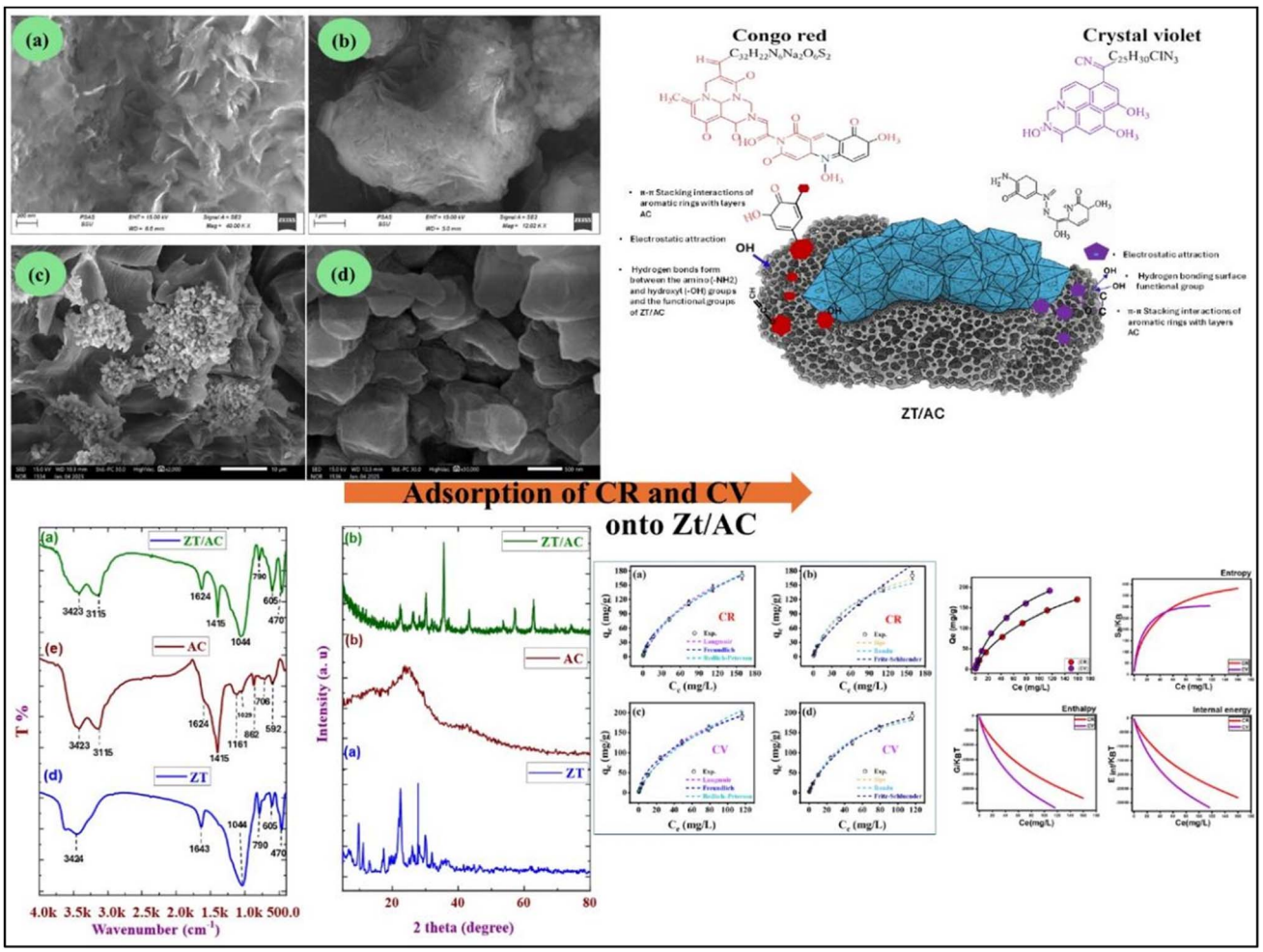

Fig. 1 Dual-dye adsorption on Zeo/AC nanocomposite: mechanism and performance.

The research addresses key gaps in the literature by developing a single material capable of handling multiple contaminants while enabling resource recovery. The material's hierarchical pore structure is engineered to optimize mass transfer and adsorption capacity by maximizing interfacial contact with the dyes. The adsorption behavior, including equilibrium and kinetics, was extensively examined. The study provides a comprehensive characterization to elucidate the synergistic mechanisms, including surface chemistry, pore structure, and electrostatic interactions, that contribute to the material's enhanced performance. Additionally, the structural integrity, stability, and recyclability of the composite were evaluated to ensure its suitability for sustainable water treatment applications. This integrated approach of simultaneous dye removal coupled with energy recovery represents a paradigm shift from conventional wastewater treatment toward sustainable resource management, offering a comprehensive solution to two significant environmental challenges within a circular economy framework (Fig. 1).

2 Materials and methods

2.1 Materials and equipment

Crystal violet (CV; $C_{25}H_{30}ClN_3$; molecular weight: 407.99 g mol^{-1}, with purity 99.92%), Congo Red (CR; $C_{32}H_{22}N_6Na_2O_6S_2$; molecular weight: 696.66 g mol^{-1}, with purity 99.95%), 37% hydrochloric acid, activated carbon and sodium hydroxide (NaOH) were obtained from Merck (Darmstadt, Germany), and deionized water (18.2 MΩ cm resistivity) was used. Clinoptilolite (Natural Egyptian zeolite ore) was kindly provided by Prof. Ahmed M. Zayed, Faculty of Science, Beni-Suef University, Egypt. This ore was collected from the north western region of Beni-Suef Governorate (N 29° 25′ 12″, E 31° 9′ 36″), Egypt. The prepared samples were analyzed *via* an Evolution 350 UV-vis Spectrophotometer (Thermo Fisher Scientific, Massachusetts, USA).

2.2 Synthesis of zeolite activated carbon (Zeo/AC) nanocomposite

The nanocomposite was synthesized through a sequential three-step protocol designed to achieve molecular-level integration and enhanced porosity. First, ball milling (Retsch PM 100; 300 rpm, 2 h) homogenized zeolite and activated carbon (2 : 1 mass ratio) using zirconia balls (10 : 1 ball-to-powder ratio) to reduce particle size and ensure interfacial contact while avoiding metallic contamination. The 2 : 1 mass ratio was optimized through preliminary experiments testing ratios from 1 : 1 to 4 : 1, with 2 : 1 demonstrating the best balance between the cation exchange capacity provided by zeolite and the high surface area contributed by activated carbon, resulting in optimal dye removal efficiency for both CR and CV. The milled mixture (30 g) underwent hydrothermal treatment (150 °C, 24 h) in a Teflon-lined autoclave after dispersion in deionized water (300 mL) and stirring (1 h), which promoted covalent bonding (*e.g.*, Si–O–C linkages) through dissolution–condensation reactions under controlled pressure/temperature. Finally, post-treatment involved filtration, washing to pH 7 (removing unreacted ions), drying (105 °C, 12 h; eliminating moisture without structural collapse), the resulting Zeo/AC nanocomposite was stored in a desiccator to preserve surface reactivity.

2.3 Material characterization

Several analytical techniques were employed to characterize the prepared adsorbent and the formed composite, including X-ray Diffraction (XRD), which utilized a PANalytical (Empyrean) instrument with Cu-Kα radiation to assess sample crystallinity, scanning from 5° to 80° at 8° min^{-1}. Fourier Transform Infrared Spectroscopy (FTIR) was conducted using a Bruker-Vertex 70 instrument *via* the KBr pellet technique, covering 400 to 4000 cm^{-1}. The tested samples were analyzed using a JEOL JSM-IT200 InTouchScope™ scanning electron microscope (JEOL Ltd, Tokyo, Japan). The particle size, polydispersity index (PDI), and zeta potential were measured with a Zetasizer Ultra (Malvern, USA) *via* dynamic light scattering (DLS) and electrophoretic light scattering.

2.4 Preparation of standard solutions of Congo red and crystal violet

The concentrations of the samples were determined spectrophotometrically using standard calibration curves. To select the analytical wavelength for the maximum absorbance method, a stock solution of each of CR and CV was prepared by diluting each in deionized water to obtain a concentration of 1000 μg mL^{-1}. Serial dilutions with different concentrations were then prepared from the stock solution using deionized water. The diluted solutions were scanned over a wavelength range of 200–400 nm using an Evolution 350 UV-vis Spectrophotometer (Thermo Fisher Scientific, Massachusetts, USA) to quantify both CR and CV contents. The maximum absorbance wavelengths (λ_{max}) were recorded at 498 nm and 590 nm for CR and CV, respectively.

2.5 Batch adsorption studies

Batch adsorption experiments were carried out to investigate the removal of CR and CV using the Zeo/AC nanocomposite. The influence of adsorbent dosage (0.025–0.20 g), contact time (0–240 min), solution pH (3–11), initial dye concentration (50–500 mg L^{-1} from a 1000 mg L^{-1} stock solution), and temperature (25, 35, 45, and 55 °C) was systematically evaluated. The selected parameter ranges were chosen to encompass environmentally relevant conditions and operational ranges for practical wastewater treatment. The pH range (3–11) covers the full spectrum from strongly acidic to alkaline conditions found in industrial effluents, while the initial dye concentration range (50–500 mg L^{-1}) represents typical concentrations in textile wastewaters. The temperature range (25–55 °C) was selected to evaluate thermodynamic behavior under both ambient and elevated temperature conditions that might be encountered in industrial processes. Unless otherwise stated, experiments were performed under standard conditions of 100 mg L^{-1} dye concentration, 50 mL solution volume, 0.1 g Zeo/AC dosage, pH 7, and 25 °C. The mixtures were agitated on an orbital shaker

(SO330-Pro) at 250 rpm for 24 h to ensure equilibrium. Initial pH values were adjusted using 0.1 N HCl or 0.1 N NaOH and measured with a calibrated pH meter (Metrohm 751 Titrino). All experiments were conducted in triplicate, and mean values were reported. After equilibration, dye-loaded Zeo/AC was separated using a 0.45 μm Millipore nylon syringe filter, and residual CR and CV concentrations were quantified by UV-vis spectrophotometry at 498 and 590 nm, respectively. Adsorption capacity (Q_e) and removal efficiency were calculated according to eqn (1) and (2):

$$Q_e\ (\text{mg g}^{-1}) = \frac{(C_o - C_e)V}{m} \quad (1)$$

$$\text{Removal}\,(\%) = \frac{100 \times (C_o - C_e)}{C_o} \quad (2)$$

where m is the mass of Zeo/AC (g), V is the volume of the CV and CR solution (L), Q_e is the amount of CV or CR adsorbed per gram (mg g^{-1}), C_o is the initial concentration of CV or CR (mg L^{-1}), and C_e is the concentration of CV or CR after adsorption (mg L^{-1}).

2.6 Traditional and advanced studies

The adsorption behaviour was investigated using a dual modelling approach combining classical and advanced models. Kinetic data were analysed using the Pseudo-First-Order (PFO), Pseudo-Second-Order (PSO), intraparticle diffusion, and Avrami models, while equilibrium data were fitted to the Langmuir and Freundlich isotherms.[30,31] Model fitting was performed through nonlinear regression, and the quality of fit was assessed using the coefficient of determination (R^2), chi-squared (χ^2), and root mean square error (RMSE), as described in eqn (3)–(5).

$$R^2 = 1 - \frac{\sum \left(q_{e,exp} - q_{e,cal}\right)^2}{\sum \left(q_{e,exp} - q_{e,mean}\right)^2} \quad (3)$$

$$\chi^2 = \sum \frac{\left(q_{e,exp} - q_{e,cal}\right)^2}{q_{e,cal}} \quad (4)$$

$$\text{RMSE} = \sqrt{\frac{\sum_{i=1}^{m} \left(Qi_{cal} - Qi_{exp}\right)^2}{m' - p}} \quad (5)$$

Thermodynamic parameters, including adsorption energy (ΔE), entropy (S_a), internal energy (E_{int}), and enthalpy (G), were calculated using eqn (6)–(9) to elucidate the adsorption mechanisms of CR and CV onto Zeo/AC at 25 °C.[32–34] Thermodynamic parameters were calculated at 25 °C to establish baseline thermodynamic behavior under standard ambient conditions, which serves as a fundamental reference point for comparison with other adsorption systems in the literature. While the optimal adsorption performance was observed at 55 °C under our experimental conditions, the 25 °C analysis provides essential thermodynamic foundation data that is particularly valuable for practical applications where ambient temperature operation is preferred for energy efficiency. This approach allows for both the determination of fundamental thermodynamic properties under standardized conditions and the evaluation of performance optimization at elevated temperatures. Entropy (S_a), derived from eqn (6), was shown to depend on the density of active sites (N_m), solute concentration (C), half-saturation concentration ($C_{0.5}$), and the number of molecules retained per site (n). Furthermore, steric parameters in combination with the translational partition function (Z_v) were applied in eqn (7) and (8) to determine internal energy (E_{int}) and enthalpy (G). Collectively, these thermodynamic descriptors provided a comprehensive understanding of the molecular interactions governing CR and CV adsorption on Zeo/AC under varying concentrations at 25 °C.

$$\Delta E = RT \ln \frac{s}{c} \quad (6)$$

$$\frac{S_a}{K_B} = N_m \left\{ \ln\left(1 + \left(\frac{C}{C_{\frac{1}{2}}}\right)^n\right) - n\left(\frac{C}{C_{\frac{1}{2}}}\right)^n \frac{\ln\left(\frac{C}{C_{\frac{1}{2}}}\right)}{1 + \left(\frac{C}{C_{\frac{1}{2}}}\right)^n} \right\} \quad (7)$$

$$\frac{E_{int}}{K_B T} = nN_m \left[\left(\frac{\left(\frac{C}{C_{\frac{1}{2}}}\right)^n \ln\left(\frac{C}{Z_v}\right)}{1 + \left(\frac{C}{C_{\frac{1}{2}}}\right)^n} \right) - \left(\frac{n \ln\left(\frac{C}{C_{\frac{1}{2}}}\right) \left(\frac{C}{C_{\frac{1}{2}}}\right)^n}{1 + \left(\frac{C}{C_{\frac{1}{2}}}\right)^n} \right) \right] \quad (8)$$

$$\frac{G}{K_B T} = nN_m \frac{\ln\left(\frac{C}{Z_v}\right)}{1 + \left(\frac{C_{\frac{1}{2}}}{C}\right)^n} \quad (9)$$

2.7 Regeneration study

To study desorption, researchers first loaded the Zeo/AC composite with dye by letting it adsorb at fixed parameters (1 h, pH 7, 0.1 g of Zeo/AC, 50 mL, 100 mg L^{-1}). The desorption studies were conducted using 0.1 g of the Zeo/AC nanocomposite, which maintained the same 2 : 1 zeolite to activated carbon mass ratio as optimized in the adsorption studies. This consistency in material composition ensures direct comparability between adsorption and desorption performance. The adsorbent mass of 0.1 g was selected as it represented the optimal dosage identified in our adsorption experiments, providing sufficient material for multiple regeneration cycles while maintaining practical experimental conditions. The dye-loaded material was then filtered, rinsed with deionized water, and dried at 105 °C for 6 h. Four different regenerants were evaluated: 0.1 M HCl (acidic), 0.1 M NaOH (alkaline), 50% ethanol (organic), and 0.1 M NaCl (saline). Desorbed dye was measured at 498 nm (CR) and 590 nm (CV), after which the adsorbent was

neutralized, dried, and reused. Reusability was tested over five adsorption/desorption cycles at pH 7, 55 °C, and 60 min.

Desorption efficiency (DE) and regeneration efficiency (RE) were determined by eqn (10) and (11):

$$\mathrm{DE}(\%) = \frac{(C_\mathrm{d} \times V_\mathrm{d})}{(Q_\mathrm{e} \times \mathrm{m})} \times 100 \quad (10)$$

$$\mathrm{RE}(\%) = \frac{Q_{\mathrm{e,n}}}{Q_{\mathrm{e},0}} \times 100 \quad (11)$$

Here, C_d(mg L^{-1}), V_d(L), Q_e(mg g^{-1}), m (g), $Q_{\mathrm{e},0}$, and $Q_{\mathrm{e,n}}$ is the desorbed CR and CV concentration, the desorption volume, the adsorption capacity, the mass of adsorbent, the initial adsorption capacity, and the adsorption capacity after cycle n, respectively.

2.8 Waste volarization section

2.8.1. Working electrode preparation. The preparation process involved dispersing 5.0 mg of the synthesized materials before and after adsorption in 485.00 μL of isopropanol containing 15.00 μL of a 5.0 wt% Nafion solution, followed by 20 minutes of sonication. A 100 μL aliquot of the prepared suspension was then drop-cast onto graphite paper (1.5 mm thick, 1 × 1 cm^2) and allowed to dry at ambient temperature.

2.8.2. Electrochemical examination. AUTO LAB PGSTAT 302 N potentiostat/galvanostat (Metrohm, Switzerland) and NOVA 1.11 software were used to record the electrochemical measurements. The reference electrode was Ag/AgCl, the counter electrode was Pt, and the working electrode was graphite in a typical three-electrode electrochemical cell operating at room temperature. To examine the electrocatalytic effectiveness of the produced electrodes, tests were conducted in a (1 M) KOH electrolyte, both with and without methanol concentration adjustment. Within the potential range of 0–1 V, CV studies were conducted at scan speeds ranging from 10 to 100 mV s^{-1}. Additionally, chronoamperometry (CA) measurements were recorded for one hour at 0.6 V. The electrochemical cell was operated as a closed system to allow controlled current flow and accurate measurement of electrochemical reactions. Cyclic voltammetry was chosen because it provides detailed information on redox processes, including reaction mechanisms and reversibility, unlike differential voltammetry which is less informative mechanistically.

2.9 Greenness assessment

Several greenness assessment tools are introduced for the evaluation for our method's sustainability and eco-friendless. The method's greenness is assessed using the AGREEprep, MoGAPI, and ComplexGAPI methods.

3 Results and discussion

3.1 Characterization of the tested materials

3.1.1. FTIR analysis. Fourier transform infrared spectroscopy was utilized to examine the functional groups and chemical alterations associated with three compounds: zeolite (Zeo), activated carbon (AC), and zeolite/activated carbon nanocomposite (Zeo/AC) (Table 1).

The FT-IR spectrum of clinoptilolite as a natural zeolite (Fig. 2a). A distinct band at 3455 cm^{-1} corresponds to the stretching vibration of (–OH) groups, while the band at 1643 cm^{-1} is assigned to the bending of interlayer H_2O. The fingerprint region illustrates characteristic framework vibrations at 1063.22 cm^{-1}, 790 cm^{-1}, 716, 605 cm^{-1}, and 470 cm^{-1}, attributed to asymmetric and symmetric stretching of (Si, Al)–O & SiO4, Si–OH, the stretching of tetrahedral TO_4 tetrahedra (T = Si, Al) stretching and O–(Si/Al)–O, respectively, consistent with zeolite structure.[30,31] Also, appearing of peak at 872.57 cm^{-1} related to Si–O.[35]

At Fig. 2b, the AC shows a broad envelope in the 3439–3115 cm^{-1} region indicative of hydroxyl (–OH) stretching. Aliphatic C–H stretching (in alkyl fragments) is reflected in the band at 2925 cm^{-1}. At 1624 cm^{-1}, a band is attributed to C=C stretching. Additional strong absorption bands at 1415, 1161, 1029, 862, 720 and 706 cm^{-1} associated with conjugated C–C/C=C interactions, C–O stretching, symmetric C–O stretching, C–Cl[36,37] and aromatic C–H out-of-plane vibrations typical of carbonaceous compounds.[32,33] Low-frequency bands that are

Table 1 FT-IR spectroscopic bands and corresponding functional groups of Zeo, AC, and ZEO/AC nanocomposite

Functional group	Zeo (cm^{-1})	AC (cm^{-1})	Zeo/AC (cm^{-1})
–OH stretching	3423	3439–3115	3439–3115
H_2O bending	1643	—	—
Aliphatic C–H stretching	—	2925	2925
C=C stretching	—	1624	1634
C–C/C=C interactions (conjugated)	—	1415	1415
C–O stretching	—	1161	—
C–O symmetric stretching	—	1029	—
Aromatic C–H out-of-plane vibrations	—	862, 706	—
C–C stretching (low-frequency)	—	592, 435	—
(Si, Al)–O asymmetric stretching	1044	—	1044
(Si, Al)–O symmetric stretching	790	—	790
TO_4 tetrahedra (T = Si, Al) stretching	605	—	605
O–(Si, Al)–O framework modes	470	—	470
Si–O–C	—	—	1218

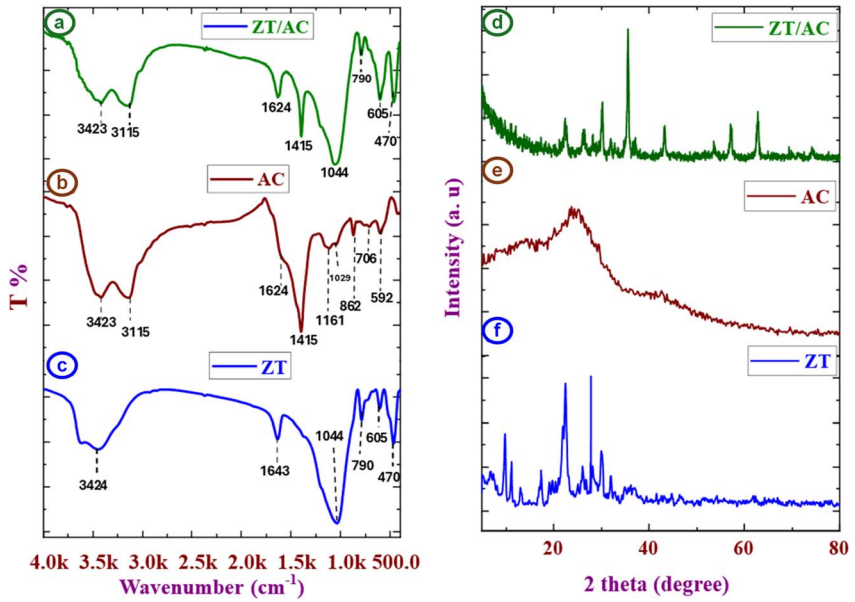

Fig. 2 FT-IR functional group analysis (a, b, and c) and XRD structural characterization (d, e, and f) of Zeo, AC, and the Zeo/AC nanocomposite, respectively.

associated with C–C stretching are located around 592 and 435 cm^{-1}.[34]

After developing the Zeo/AC nanocomposite, the zeolite framework bands are retained at 470, 605, 790, and 1044 cm^{-1}, confirming preservation of the (Si, Al)–O and TO_4 tetrahedra (T = Si, Al) stretching functionalities (Fig. 2c).[38,39] In Zeo/AC nanocomposite, the broad band in AC envelope stretching 1311 : 1641 cm^{-1} becomes resolved into two sharper bands at 1395.20 and 1634 cm^{-1}, indicating better-defined contributions from C–O/C–C and C=C vibrations, respectively. While remaining in comparable locations, the regions 3439 : 3115 cm^{-1} (–OH) and 2925 cm^{-1}, aliphatic C–H, exhibit variations in intensity.[39,40] Overall, the persistence of zeolite framework bands alongside AC-derived features with modest shifts and intensity variations and the disappearance of some bands corroborates successful Zeo/AC nanocomposite formation. As shown in Fig. 2 the peak appeared at 1399.50 cm^{-1} in AC sample shifted to 1390.20 cm^{-1} in composite sample are shifted and change in the peak intensity and the decrease in broadining which may be related to Al–O and C–O interaction to form Al–O–C[41] Fig. S2.

Si–O–C bonds in zeolite/activated carbon composites represent chemical linkages formed between silicon, oxygen, and carbon atoms, creating a hybrid interface between the zeolite framework and the activated carbon surface (Fig. S1). These bonds influence the surface chemical properties and are sensitive to the preparation conditions. In the FTIR spectrum, a small, low-intensity peak appears around 1218 cm^{-1}, attributed to Si–O–C asymmetric stretching vibrations within the silica-carbon network. Such Si–O–C bonds play a vital role in linking the silica structure of the zeolite with the carbon surface, impacting functional groups and surface chemistry. Chemically or physically treated activated carbons develop oxygen-containing groups that interact with silicon species from the zeolite to form Si–O–C bonds, which affect surface heterogeneity and adsorption characteristics. Additionally, silicon oxycarbide (SiOC) materials synthesized *via* mechanochemical methods integrate Si, O, and C atoms into thermally stable, porous networks that are valuable as catalyst supports and adsorbents.[42] This chemical interaction was confirmed by performind physical preparation of zeolite-activated carbon composites involves simple mixing of the two materials with weak physical interactions. It is quick and easy but may result in less stable and non-uniform composites which probably shown in Fig. S2.

3.1.2. XRD analysis. X-ray diffraction (XRD) was performed to analyze the structural and phase composition of AC, Zeo, and Zeo/AC nanocomposite. The XRD patterns, shown in (Fig. 2d), confirmed the presence of clinoptilolite, natural type of zeolite, based on Card Nos. JCPDS 00-025-1349 and 01-079-1460 with characteristic peaks (020), (200), (–201), (111), (–131), (–421), (–222), (151) and (–602) can be indexed at $2\theta = 9.77°$, 11.2°, 13.9°, 17.3°, 19.5°, 22.8°, 26°, 30.1°, and 32.67°, respectively.[35,43] The results revealed that the pure zeolite sample was indeed clinoptilolite, with a small average crystallite size of 3.09 nm.[44]

The diffractogram of AC showed two broad peaks at 24.4° and 43°, characteristic of amorphous carbon (Fig. 2e). For the AC, the diffractogram showed two broad, amorphous peaks at 24.4° and 43°, which are typical of disordered aromatic carbon and graphitic domains, respectively. A peak at 24.67° also indicated the presence of activated carbon. The XRD pattern of the Zeo/AC nanocomposite showed a decrease in the intensity of the zeolite peaks, additionally, new or enhanced peaks at 22.3° and 27° and a significantly larger crystallite size of 30.49 nm, providing evidence of a well-formed Zeo/AC nanocomposite (Fig. 2e).[45]

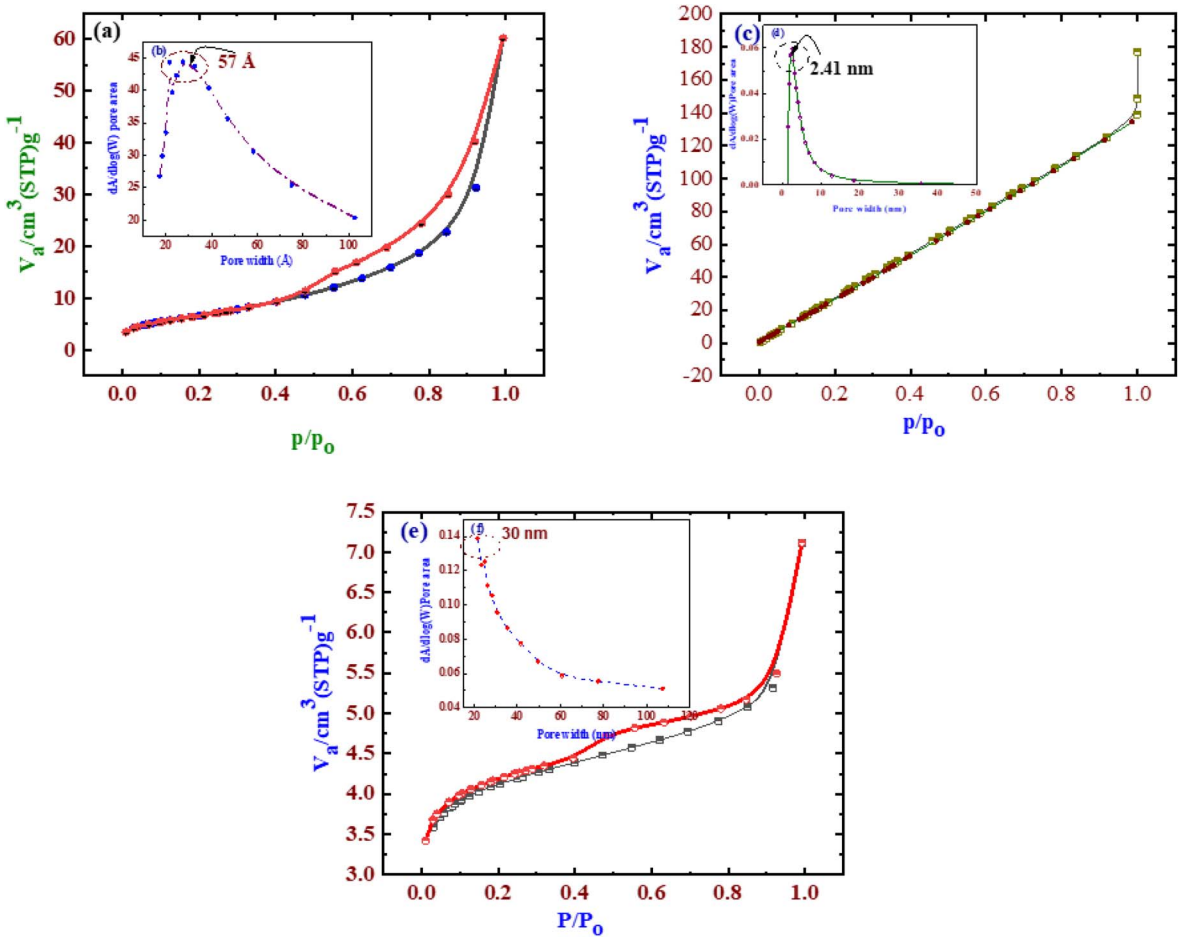

Fig. 3 BET surface area and pore structure analyses of AC (a), Zeo (c), and Zeo/AC (e). (b), (d), and (f) are inset figures in (a), (c), and (e) showing the pore size distribution curves.

3.1.3. Textural characteristics. To evaluate the textural characteristics such as specific surface area and pore size distribution, nitrogen (N_2) adsorption–desorption isotherm analysis was carried out. As shown in (Fig. 3), the adsorption–desorption profiles of AC, Zeo, and Zeo/AC display type IV isotherms, which are indicative of mesoporous materials. The presence of H4-type hysteresis loops in all samples suggests that the mesopores arise from slit-like structures typically formed by layered or lamellar particles.[46]

Additionally, (Fig. 3c) illustrates the N_2 adsorption–desorption behavior of the zeolite sample, highlighting its surface area, pore volume, and pore size. Based on IUPAC standards, clinoptilolite-type zeolites exhibit type IV isotherms with H3-type hysteresis loops.[39] The H3 loop is associated with aggregates of plate-like particles that form slit-shaped pores of varying size, consistent with the morphology observed in SEM images.[47] The zeolite exhibited a surface area of 23.6218 $m^2\ g^{-1}$, a pore volume of 0.091066 $cm^3\ g^{-1}$, and a dominant pore diameter of approximately 14.7 nm, indicating the coexistence of mesoporous and macroporous structures. This was further confirmed by BJH analysis, which supported the mesoporous nature suggested by BET measurements.

According to Table 2, the specific surface areas of AC, Zeo, and Zeo/AC were 302.3951 $m^2\ g^{-1}$, 23.6218 $m^2\ g^{-1}$, and 225.37 $m^2\ g^{-1}$, respectively. The significant increase in surface area observed for Zeo/AC compared to Zeo alone indicates that incorporating Zeo into AC helps prevent excessive stacking of LDH layers, thereby improving porosity. Owing to its enhanced pore structure, Zeo/AC shows strong potential for application in water treatment technologies.

The colloidal properties of the adsorbent materials, namely surface charge and particle size distribution, were critically evaluated to elucidate their anticipated performance in the simultaneous removal of cationic and anionic dyes at (Fig. 4). The pristine Zeo exhibited a zeta potential of −13.5 mV (Fig. 4a), a moderate negative surface charge characteristic of its aluminosilicate framework. This charge, while favorable for attracting cationic species like CV, suggests limited colloidal stability, a fact corroborated by its Z-average hydrodynamic diameter of 420.7 nm (Fig. 4c), which indicates significant aggregation in suspension. In stark contrast, the Zeo/AC carbon composite demonstrated a markedly enhanced negative zeta potential of −28.7 mV (Fig. 4b). This profound increase in surface negativity is directly attributable to the introduction of oxygen-rich functional groups from the activated carbon component. A zeta

Table 2 Textural properties of AC, Zeo, and Zeo/AC

Material	BET surface area ($m^2\ g^{-1}$)	Total volume of pores ($cm^3\ g^{-1}$)	The mean diameter of pores (based on BHJ) (nm)
AC	302.3951	0.245238	3.244
Zeo	23.6218	0.0911	14.785
Zeo/AC	225.37	0.2130	3.7738

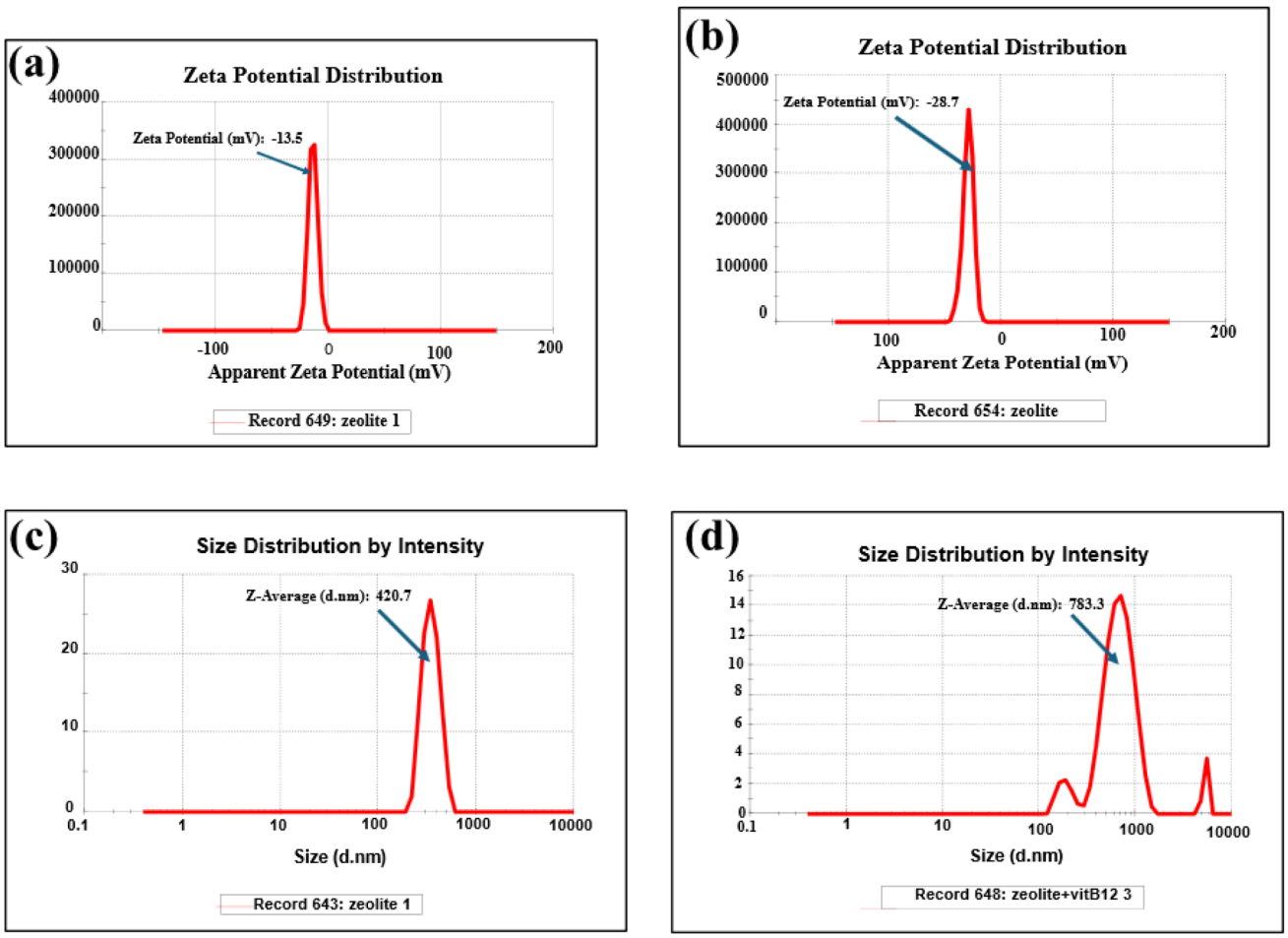

Fig. 4 Zeta potential images of (a and c) for Zeo and Zeo/AC and particle size distribution (b and d) of Zeo and Zeo/AC.

potential beyond ±25 mV signifies excellent electrostatic stabilization, which is paramount for maintaining a high active surface area in aqueous treatment systems.

Concurrently, the DLS analysis revealed a larger Z-average diameter of 783.3 nm for the Zeo/AC. This increase is not indicative of further aggregation but is instead consistent with the successful formation of a hybrid material (Fig. 4d). The larger apparent size can be attributed to the intrinsic porosity and micron-scale dimensions of the integrated AC, which creates a more extensive, accessible surface architecture. This combination of a highly negative surface charge and a larger, stable structure presents a compelling mechanism for dual-function dye adsorption. The enhanced negative charge will potentiate stronger electrostatic interactions with the cationic CV molecules, thereby likely increasing its adsorption capacity. Conversely, for the anionic CR, the increased surface area and porosity provided by the AC become the dominant factors, facilitating adsorption primarily through non-electrostatic interactions such as π–π stacking and hydrogen bonding. Thus, the composite's design successfully merges the ion-exchange capability of zeolite with the high surface area and surface functionality of activated carbon, creating a versatile adsorbent tailored for the treatment of complex wastewater containing dyes of opposing charges.

The morphology of synthesized materials is visualized using SEM. The Zeolite particles exhibited crystalline morphology, exhibiting well-defined, angular particles with a relatively smooth surface texture. The particles appear aggregated into larger

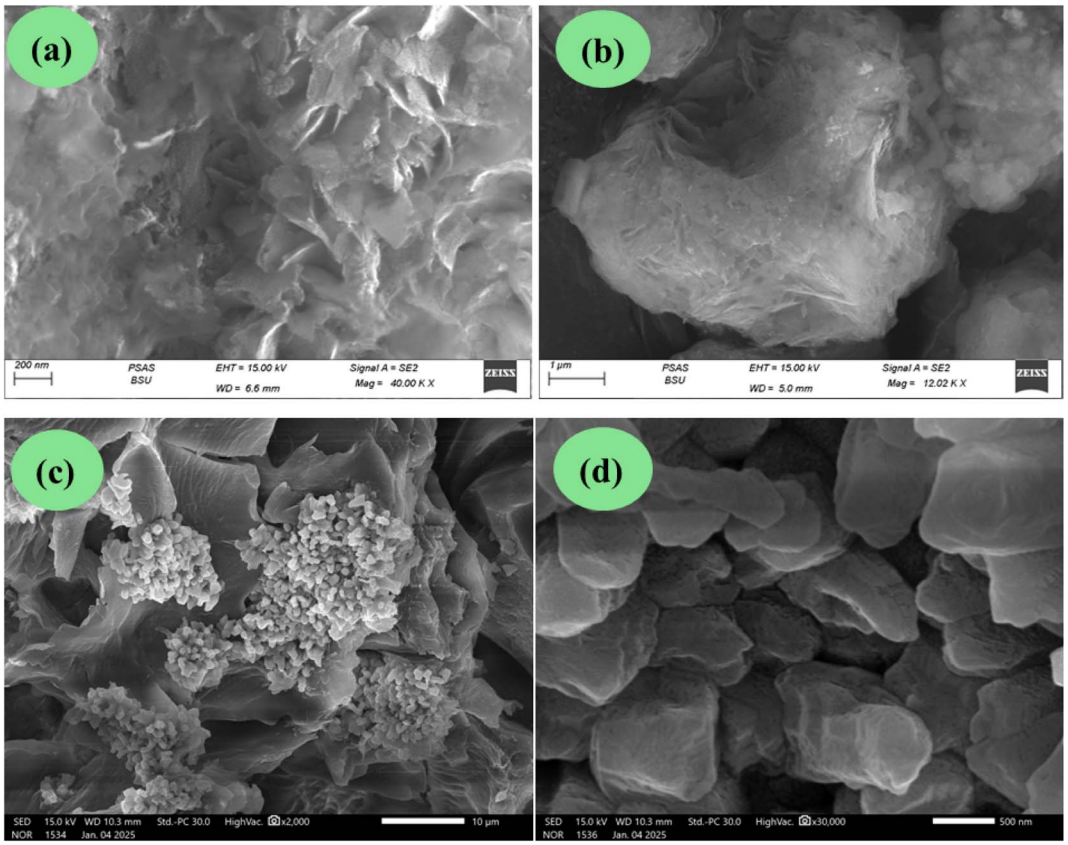

Fig. 5 SEM micrographs of (a and b) Zeo and (c and d) Zeo/AC.

clusters, consistent with the particle size distribution data indicating limited colloidal stability (Fig. 5a and b). This aggregation reduces the accessible surface area, which may limit adsorption efficiency. The microporous suggesting a potential for molecular sieving and ion-exchange a property beneficial for capturing cationic dyes like Crystal Violet *via* electrostatic interactions.[48,49] In contrast, the composite material demonstrates a markedly different morphology. The integration of activated carbon in (Fig. 5c and d) results in a heterogeneous, highly porous, and roughened surface architecture. The zeolite particles appear dispersed within a fibrous, amorphous carbon matrix, which introduces meso- and macropores. This hierarchical pore structure is ideal for facilitating diffusion and adsorption of larger dye molecules such as CR and CV. The enhanced surface roughness and increased porosity align with the larger hydrodynamic diameter observed in DLS, confirming that the composite's structure provides more active sites and reduced mass transfer resistance during adsorption.

The morphological features of the 2 materials (Zeo, and Zeo/AC) were noticeably changed by the hybridization method. As shown in the SEM images (Fig. 5a and b), these changes were observed on both the surface and in the internal structure of the Zeo during the modification step by AC. The SEM images of raw zeolite (Zeo) show an irregular and rough surface morphology with agglomerated plats (Fig. 5a), at higher magnification, reveals clusters of flaky compacted grains with sharp edges, while (Fig. 5b) illustrates a more compact three-dimensional agglomerated structures, indicating the commonly typical crystalline morphology of zeolite minerals. This morphology provides limited surface accessibility, which may restrict adsorption capacity in its pristine state. The SEM of the Zeo/AC nanocomposite display a distinct change in surface texture (Fig. 5c and d). Fig. 5c shows AC particles well-distributed on the surface, forming small, spherical clusters or agglomerates scattered across a larger surface which creating a porous, heterogeneous structure. In (Fig. 5d), it denotes diminutive, blocky, granular particles characterized by rough edges and increased porosity. The significant difference in the morphology and size of Zeo/AC relative to zeolite indicates that the hybridization approach has effectively developed a novel porous nanocomposite, improving its adsorption efficiency.

3.2 Optimization of adsorption parameters

3.2.1. Effect of solution pH. The pH optimization study revealed that maximum adsorption efficiency for both Congo red and crystal violet was achieved at pH 7.0, as shown in (Fig. 6a). This optimal pH can be rationalized by considering dye speciation, adsorbent surface charge, and electrostatic interactions, as demonstrated in recent mechanistic studies by Fernández-Andrade *et al.* (2021) on multi-dye adsorption systems.[50]

To elucidate the role of surface charge in the adsorption mechanism, the point of zero charge (pHpzc) of the Zeo/AC nanocomposite was determined to be 6.1 using the pH drift

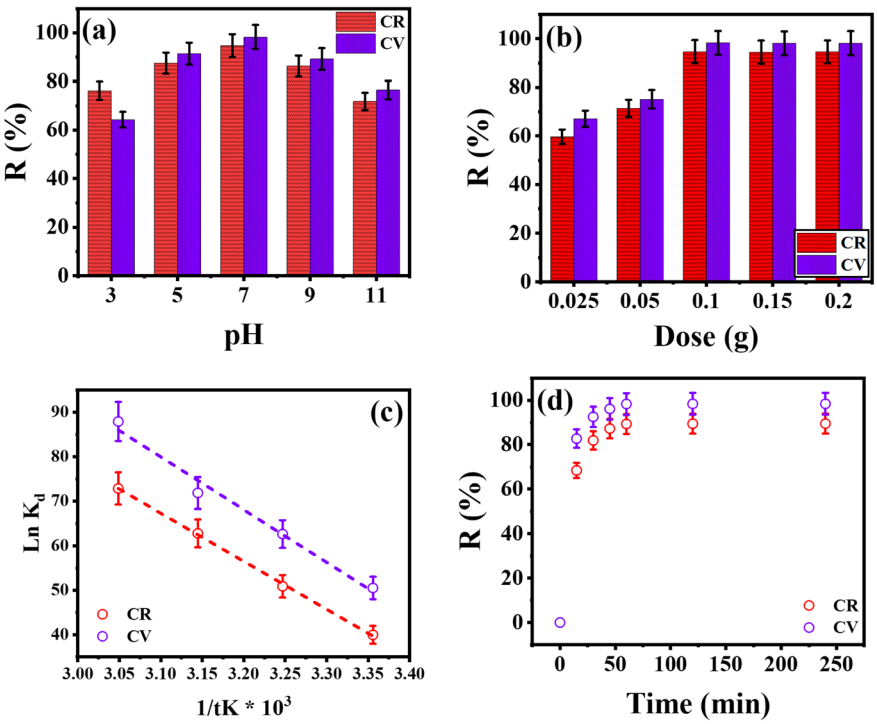

Fig. 6 Effect of adsorption parameters on Congo red and crystal violet removal by Zeo/AC nanocomposite; (a) influence of solution pH on removal percentage; maximum efficiency is observed at pH 7, (b) effect of adsorbent dose on removal efficiency; optimal performance at 0.1 g/50 mL, (c) temperature dependence of adsorption capacity (q_e); capacity increases with temperature, optimal at 328.15 K (25 °C). And (d) contact time profiles (q_e); equilibrium achieved within 60 minutes for both dyes.

method. This value indicates that the adsorbent surface is positively charged at pH < 6.1 due to protonation of surface functional groups, and negatively charged at pH > 6.1 due to deprotonation. The methodology aligns with established protocols described by Nazari *et al.* (2022) for composite adsorbents.[51] Notably, the pHpzc value of 6.1 is intermediate between that of pristine activated carbon (typically pH 8–10) and natural zeolite (typically pH 4–6), suggesting successful integration of the two materials and supporting the synergistic behavior of the hybrid composite. Similar intermediate values have been reported by several studies for zeolite-carbon composites, corroborating the present findings.[52–54] This intermediate pHpzc is pivotal for the simultaneous adsorption of the two oppositely charged dyes at a neutral pH of 7.0. At this pH, the Zeo/AC surface carries a slight net negative charge (pH > pHpzc), which has distinct implications for each pollutant where Congo red, with a pKa of 4.5,[47] exists predominantly in its anionic form (CR^-) at pH 7.0. At this pH, the slightly negative surface of the Zeo/AC nanocomposite creates an initial electrostatic repulsion with the anionic CR^- ions. The high adsorption efficiency achieved despite this repulsion underscores that non-electrostatic interactions such as hydrogen bonding, π–π stacking, van der Waals forces, and pore filling are the dominant mechanisms for Congo red removal. The relatively high adsorption efficiency, despite electrostatic repulsion, highlights the role of these alternative mechanisms, consistent with findings by Pham *et al.* (2020) on anionic dye adsorption using composite materials.[55]

Crystal violet, a diprotic cationic dye with pKa values of 5.31 and 8.64, exists mainly as a monovalent cation (CV^+) at pH 7.0. Under these conditions, the slightly negatively charged surface of the Zeo/AC nanocomposite (pH > pHpzc) promotes a favorable electrostatic attraction for the CV^+ cations. This electrostatic interaction acts synergistically with π–π stacking between the dye's aromatic rings and the carbon component of the composite, significantly enhancing the adsorption capacity and kinetics for the cationic dye.[56] These combined interactions contribute to enhanced adsorption capacity. Ali Khan *et al.* (2021) reported similar pH-responsive behavior in carbon-based systems for cationic dye adsorption.[57]

Overall, the intermediate pHpzc of the Zeo/AC composite enables effective adsorption of both anionic and cationic dyes across a broader pH range than the individual components. Specifically, it allows for favorable electrostatic binding of cationic crystal violet while still facilitating high-capacity removal of anionic Congo red through superior surface chemistry and porosity, despite initial electrostatic repulsion. The observed adsorption efficiency within a pH range of 6–8 suggests robust performance under realistic environmental conditions, such as variable pH in actual wastewater, aligning with trends reported by several studies for mixed dye systems on composite adsorbents.[48,58]

3.2.2. Effect of adsorbent dosage. Optimization of adsorbent dosage revealed that 0.1 g of Zeo/AC nanocomposite per 50 mL solution provided optimal adsorption performance for both dyes, as shown in (Fig. 6b). This corresponds to an

adsorbent concentration of 2.0 g L^{-1}, which represents a balance between maximum dye removal efficiency and economic considerations. The dosage range of 0.025–0.20 g (0.5–4 g L^{-1}) was selected based on preliminary screening tests that identified this as the optimal range where significant changes in removal efficiency could be observed while maintaining practical relevance for industrial applications. The dosage optimization approach follows methodologies established by Adeleke *et al.* (2017) for composite adsorbent systems.[49,59]

Increasing the adsorbent dose beyond 0.1 g resulted in minimal improvement in removal efficiency, indicating saturation of available adsorption sites. This behavior is characteristic of Langmuir-type adsorption, where a monolayer coverage limit exists. Conversely, doses below 0.1 g showed significantly reduced removal efficiency due to insufficient adsorption sites relative to dye concentration.[49,60]

3.2.3. Effect of temperature. Temperature optimization studies conducted across the range of 25 °C to 55 °C revealed that maximum adsorption capacity was achieved at 55 °C, as shown in (Fig. 6c). This temperature dependence indicates that the adsorption process is endothermic in nature, with higher temperatures promoting increased molecular mobility and enhanced dye–adsorbent interactions. The endothermic behavior is consistent with reports by Hasanzadeh *et al.* (2020) for organic dye adsorption on porous composites.[61]

The positive temperature effect can be attributed to several factors including increased kinetic energy enhancing dye molecule mobility and access to internal pore structures, potential activation of additional adsorption sites through thermal expansion of the adsorbent matrix, and weakening of hydration shells around dye molecules, facilitating their interaction with adsorbent surfaces. These mechanisms have been extensively discussed by several studies in their thermodynamic analysis of composite adsorbent systems.[62,63]

Thermodynamic analysis of the temperature-dependent data revealed positive values for enthalpy change ($\Delta H°$), confirming the endothermic nature of the adsorption process. The positive entropy change ($\Delta S°$) suggests increased randomness at the solid–liquid interface during adsorption, possibly due to displacement of water molecules and structural rearrangements, as illustrated in Table S1. Similar thermodynamic parameters have been reported by several studies for dye adsorption on hierarchical porous materials.[64–66]

The optimal temperature of 55 °C represents a practical compromise between adsorption efficiency and energy requirements. While higher temperatures might further enhance adsorption, the marginal improvement would not justify the additional energy costs in industrial applications.

3.2.4. Contact time and kinetic analysis. The contact time optimization revealed that adsorption equilibrium was achieved within 60 minutes for both Congo red and crystal violet, as illustrated in (Fig. 6d). This rapid equilibration indicates efficient mass transfer characteristics of the Zeo/AC nanocomposite, attributed to its hierarchical pore structure and intimate mixing of components. The kinetic behavior is consistent with findings by Durán-Egido *et al.* (2025) for composite adsorbents with optimized pore structures.[67]

3.2.5. Adsorption isotherms. To better understand the interaction between the Zeo/AC nanocomposite and the dye molecules, equilibrium data were analyzed using several well-established adsorption isotherm models. These included two-parameter models such as Langmuir and Freundlich, three-parameter models like Sips and Redlich-Peterson, and more complex four-parameter models including Fritz–Schlunder and Baudu. Each model provides a unique perspective on the adsorption process, ranging from assumptions of monolayer adsorption on homogeneous surfaces to heterogeneous, multilayer adsorption involving complex site distributions. The selection of these models allowed for a comprehensive evaluation of the adsorption mechanisms governing the removal of CR and CV under optimized conditions, as illustrated in Table 3 and (Fig. 7).

The isotherm studies were conducted at a fixed temperature of 25 °C, pH 7.0, with 0.1 g of Zeo/AC in 50 mL dye solution, across an initial concentration range of 5–500 mg L^{-1}. Nonlinear regression fitting was employed to extract model parameters and assess the goodness of fit (R^2), ensuring accurate interpretation of the adsorption behavior.

For CR, the Langmuir model yielded a maximum monolayer capacity (q_m) of 728.3 ± 5.8 mg g^{-1} with a strong correlation coefficient ($R^2 = 0.998$), supporting the assumption of uniform adsorption sites. The Freundlich model indicated surface heterogeneity and multilayer formation ($n = 2.84 \pm 0.08$), though with a slightly lower R^2 value (0.977). The Redlich–Peterson and Sips models provided improved fitting, with the Sips model offering an excellent fit ($q_m = 745.2 \pm 6.1$ mg g^{-1}; $R^2 = 0.999$), highlighting a combined mechanism of homogeneous and heterogeneous adsorption. The four-parameter Fritz–Schlunder model further refined the prediction ($q_m = 738.5 \pm 5.5$ mg g^{-1}; $R^2 = 0.999$), while the Baudu model estimated the highest capacity ($q_0 = 752.6 \pm 6.3$ mg g^{-1}; $R^2 = 0.997$), reflecting the complex nature of CR adsorption.

Similarly, CV exhibited superior fit with the Langmuir model ($q_m = 879.2 \pm 6.4$ mg g^{-1}; $R^2 = 0.999$), indicating monolayer coverage on a uniform surface. The Freundlich model also captured key aspects of the process ($n = 3.02 \pm 0.09$; $R^2 = 0.972$), suggesting favorable adsorption and surface heterogeneity. As with CR, the three-parameter models showed high accuracy, with the Sips model again offering the best performance ($q_m = 895.7 \pm 7.2$ mg g^{-1}; $R^2 = 0.999$). The Fritz–Schlunder model closely approximated this capacity ($q_m = 886.4 \pm 6.8$ mg g^{-1}; $R^2 = 0.999$), and the Baudu model predicted the highest uptake ($q_0 = 908.3 \pm 7.5$ mg g^{-1}; $R^2 = 0.998$).

Overall, the exceptional agreement between experimental and theoretical values, especially in the Sips and Fritz–Schlunder models ($R^2 > 0.999$), suggests the presence of multiple adsorption mechanisms. These likely involve electrostatic interactions provided by the zeolite fraction and π–π stacking contributed by the activated carbon. Furthermore, the observed increase in adsorption capacity at elevated temperatures aligns with an endothermic process, as previously supported by thermodynamic analysis.

Table 3 Nonlinear isotherm model parameters for Congo Red (CR) and Crystal Violet (CV) adsorption onto Zeo/AC at 55 °C

Model	Parameter	Congo Red (CR)	R^2 (CR)	Crystal Violet (CV)	R^2 (CV)
Langmuir	q_m (mg g^{-1})	728.3 ± 5.8	0.998	879.2 ± 6.4	0.999
	K_L (L mg^{-1})	0.042 ± 0.001		0.051 ± 0.001	
Freundlich	K_F (mg g^{-1}) (L mg^{-1}) n	124.6 ± 3.2	0.977	158.3 ± 3.8	0.972
	n	2.84 ± 0.08		3.02 ± 0.09	
Redlich–Peterson	K_{RP} (L g^{-1})	32.7 ± 0.9	0.996	46.2 ± 1.2	0.995
	a_{RP} (L mg^{-1})	0.078 ± 0.002		0.091 ± 0.002	
	β	0.93 ± 0.02		0.95 ± 0.02	
Sips	q_m (mg g^{-1})	745.2 ± 6.1	0.999	895.7 ± 7.2	0.999
	K_S (L mg^{-1})	0.036 ± 0.001		0.044 ± 0.001	
	n	1.12 ± 0.03		1.08 ± 0.03	
Fritz–Schlunder	q_m (mg g^{-1})	738.5 ± 5.5	0.999	886.4 ± 6.8	0.999
	K_{FS} (L mg^{-1})	0.048 ± 0.001		0.057 ± 0.001	
	a_{FS}	0.052 ± 0.001		0.063 ± 0.001	
	β	0.97 ± 0.02		0.94 ± 0.02	
Baudu	q_0 (mg g^{-1})	752.6 ± 6.3	0.997	908.3 ± 7.5	0.998
	K_b (L mg^{-1})	0.029 ± 0.001		0.035 ± 0.001	
	b (L^2 mg^{-2})	0.0011 ± 0.0001		0.0013 ± 0.0001	

In conclusion, the high uptake capacities, strong model fitting, and rapid equilibrium kinetics (achieved within 60 minutes) collectively affirm the potential of the Zeo/AC nanocomposite for scalable and efficient dye removal in environmental remediation efforts.

3.2.6. Adsorption kinetics. To gain insights into the adsorption behavior of Congo Red (CR) and Crystal Violet (CV) onto the Zeo/AC nanocomposite, the kinetic data were analyzed using four models: pseudo-first-order (PFO), pseudo-second-order (PSO), Avrami fractional-order, and intraparticle diffusion (IPD), refer to (Fig. 8). The nonlinear models' parameters are summarized in Table 4.

The pseudo-first-order model showed a weaker fit for both CR and CV, as indicated by lower R^2 values and large deviations between the experimental and calculated adsorption capacities. This suggests that physisorption or reversible diffusion-controlled processes are not the predominant mechanisms for dye uptake in this system.

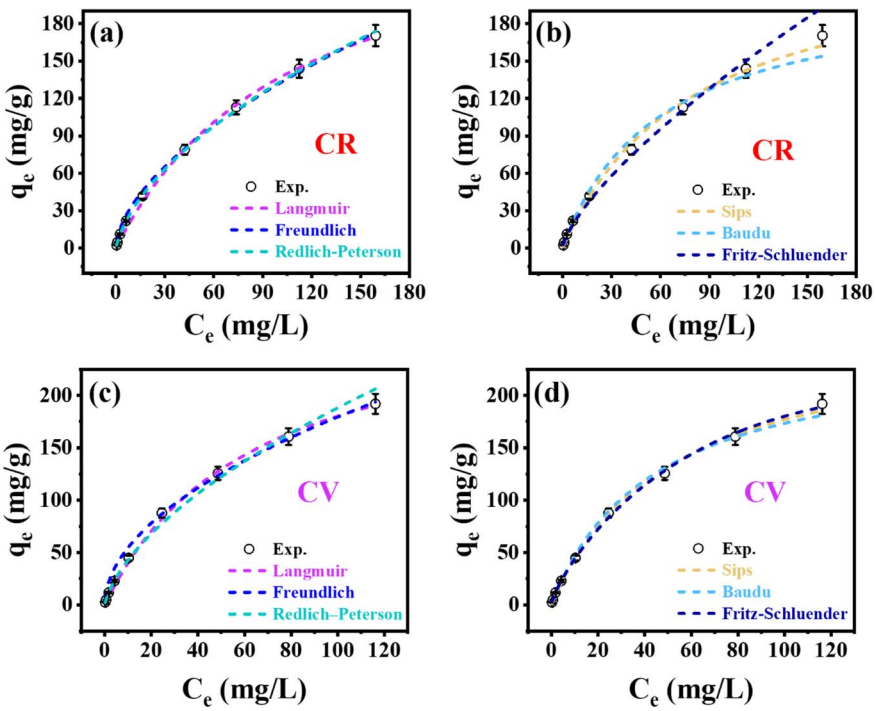

Fig. 7 Adsorption isotherms for Congo Red (CR) and Crystal Violet (CV) on zeolite/activated carbon nanocomposite at 55 °C and pH 7.0. Experimental data (circles) fitted with different isotherm models: (a and b) CR adsorption and (c and d) CV adsorption. Models include Langmuir, Freundlich, Redlich-Peterson (a and c), and Sips, Baudu, Fritz-Schluender (b and d). All models show excellent fit with R^2 > 0.97, indicating complex adsorption mechanisms involving both monolayer and multilayer processes.

In contrast, the pseudo-second-order model exhibited the best fit, with the highest correlation coefficients ($R^2 > 0.998$) and excellent agreement between experimental and theoretical q_e values. This confirms that the adsorption process is governed by chemisorption, likely involving electron sharing or exchange between the functional groups on the Zeo/AC surface and the dye molecules.

The Avrami fractional-order model also demonstrated a strong fit, supporting the presence of heterogeneous and multi-pathway adsorption kinetics. The Avrami exponent (n) ranged between 0.74 and 0.91, indicating a decelerating adsorption rate and the involvement of multiple sorption mechanisms occurring simultaneously.

To further understand the diffusion mechanism, the intra-particle diffusion model was employed. The q_t *versus* $t^{0.5}$ plots revealed three distinct linear stages. The initial region reflects external film diffusion, followed by a gradual adsorption phase corresponding to intraparticle diffusion, and finally a plateau representing equilibrium. Since the plots did not pass through the origin, intraparticle diffusion is not the sole rate-limiting step. Notably, the intercepts (C values) were higher for CV than CR, indicating a greater boundary layer effect and higher external mass transfer resistance for the larger CV molecules. The kinetic data confirm that the adsorption of both CR and CV onto Zeo/AC follows a chemisorption-controlled process, with contributions from boundary layer diffusion and intraparticle transport. The strong performance of the Avrami model further supports the complexity and heterogeneity of the adsorption mechanism. Critically, the rapid equilibrium achieved within 60 minutes for both dyes is a significant practical finding, underscoring the material's high efficiency and potential for the simultaneous treatment of mixed-dye waste streams without requiring extended retention periods.

3.2.7. Steric parameters

3.2.7.1. Number of adsorbed ions per site. The number of adsorbed ions per site (n) provides insight into the orientation and interaction mechanisms of CR, and CV ions on Zeo/AC surfaces. If $n < 1$, adsorption follows a horizontal orientation,

Table 4 Nonlinear kinetic parameters for CR and CV adsorption onto Zeo/AC nanocomposite at 55 °C

Model	Parameter	CR	CV
Pseudo-first-order	$q_{e,cal}$ (mg g^{-1})	50.61	72.42
	k_1 (min^{-1})	0.031	0.026
	R^2	0.964	0.957
Pseudo-second-order	$q_{e,cal}$ (mg g^{-1})	58.21	79.66
	k_2 (g mg^{-1} min^{-1})	0.0019	0.0021
	R^2	0.998	0.999
Avrami fractional order	$q_{e,cal}$ (mg g^{-1})	57.93	78.45
	k_{av} (min^{-1})	0.051	0.047
	n	0.74	0.91
	R^2	0.993	0.995
Intraparticle diffusion	k_{id1} (mg g^{-1} min$^{-0.5}$)	3.61	5.82
	C_1 (mg g^{-1})	20.43	33.77
	R_1^2	0.982	0.987
	k_{id_2}	1.62	2.48
	C_2	31.84	44.05
	R_2^2	0.944	0.951
	k_{id_3}	0.21	0.39
	C_3	48.59	63.57
	R_3^2	0.881	0.912

meaning multiple ions occupy a single active site, forming multi-ionic interactions.[68–70] For CR, the $n = 0.78$ and for CV, the $n = 0.83$ (Table 5). Since n values <1, this suggests that CR, and CV ions exhibit multi-ionic interactions during adsorption. Each adsorption site can hold up to one CR ions and one CV ions, with ions aligning horizontally arrangement.[70,71]

3.2.7.2. Occupied active sites density and saturation adsorption capacity. The N_m parameter represents the density of adsorption sites on the Zeo/AC surface, providing insight into the total number of binding sites available for CR and CV ions (Table 5). CR adsorption site densities (N_m) were 576 mg g^{-1} at 298 K superior to CV where N_m of = 439, increased aggregation of CR ions than CV on available sites.[72,73] The saturation adsorption capacity (Q_{sat}) represents the maximum potential for metal ion adsorption onto Zeo/AC. Its value is influenced by both N_m (density of occupied sites) and n (number of ions per

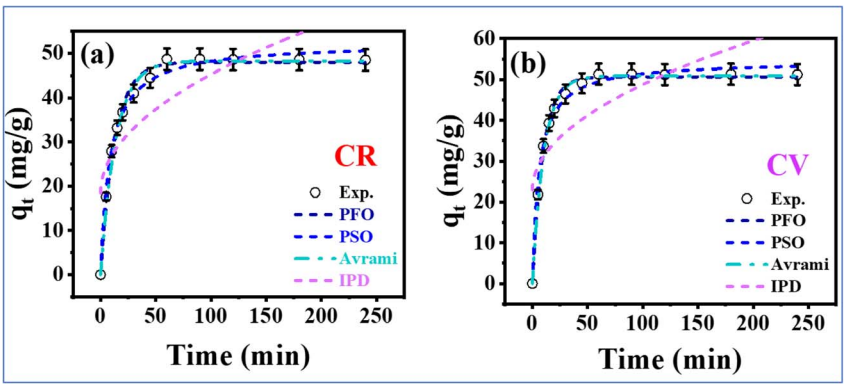

Fig. 8 Adsorption kinetics of (a) Congo Red (CR) and (b) Crystal Violet (CV) on zeolite/activated carbon nanocomposite using different kinetic models including pseudo-first-order (PFO), pseudo-second-order (PSO), Avrami fractional-order, and intraparticle diffusion (IPD). The PSO model shows the best fit ($R^2 > 0.998$), indicating chemisorption-controlled adsorption with rapid equilibrium achieved within 60 minutes for both dyes.

Table 5 Steric Parameters for CR and CV adsorption onto Zeo/AC nanocomposite at 298 K

		CR	CV
298 K	R^2	0.9996	0.9992
	χ^2	0.018	0.052
	n	0.78	0.83
	N_m (mg g^{-1})	576	439
	Q_{sat} (mg g^{-1})	451	365
	$C_{1/2}$ (mg L^{-1})	300	104
	ΔE (kJ mol^{-1})	−10.9	−12.4

site). The estimated CR adsorption capacities (Q_{sat}) were 451 mg g^{-1} at 298 K, and for the CV adsorption capacities, the computed values were 365 mg g^{-1} (Table 5). The temperature-dependent variation in Q_{sat} is more closely linked to changes in N_m (occupied site density) rather than n (ions per site). This suggests that the number and availability of active sites play a more critical role in determining adsorption efficiency than the adsorption capacity of individual sites where n of CV (0.83) more than n of CR (0.78) but N_m of CR (576) more than CV (439) at same temperature.[72,74]

3.2.7.3. Adsorption energy. The adsorption energy (ΔE) plays a crucial role in identifying the fundamental mechanisms governing the adsorption of CR and CV on the Zeo/AC surface. It allows for differentiation between physical and chemical adsorption processes. Generally, chemical adsorption is characterized by energy values exceeding 80 kJ mol^{-1}, whereas physical adsorption involves lower energy values, typically 40 kJ mol^{-1} or less. Within physical adsorption, specific interaction types can be categorized based on their energy ranges: coordination exchange (~40 kJ mol^{-1}), hydrogen bonding (<30 kJ mol^{-1}), dipole interactions (2–29 kJ mol^{-1}), van der Waals forces (4–10 kJ mol^{-1}), and hydrophobic bonds (~5 kJ mol^{-1}).[74,75] The adsorption energy values for CR and CV were calculated using eqn (6), which incorporates thermodynamic parameters, including the solubility of dye (CR and CV) in water (S), gas constant ($R = 0.008314$ kJ mol^{-1} K^{-1}), absolute temperature (T), and ion concentration at half-saturation.

The obtained energy ranges were up to −10.9 kJ mol^{-1} for CR, and for CV = −12.4 kJ mol^{-1} (Table 5). These results strongly indicate that the adsorption of these dyes onto Zeo/AC is predominantly driven by physical adsorption mechanisms, including van der Waals forces, hydrophobic interactions, dipole interactions, and hydrogen bonding. The consistently negative ΔE values further validate that the adsorption process is exothermic, aligning with previous.

3.2.8. Thermodynamic functions

3.2.8.1. Entropy. Entropy (S_a) provides valuable insight into the structural order–disorder transitions occurring on the Zeo/AC surface during CR and CV adsorption. Analysis of S_a (eqn (9)), based on steric parameters such as the density of occupied sites (N_m), the number of ions per site (n), and the half-saturation concentration ($C_{0.5}$), revealed a slight decline in entropy with increasing ion uptake, particularly at higher concentrations (Fig. 9b). This reduction reflects decreased surface disorder, indicating that as adsorption sites become progressively occupied, the structural mobility of the adsorbent diminishes.[72] Such behavior supports the spontaneous character of adsorption, as ions become increasingly restricted upon binding to the Zeo/AC surface. The observed entropy decrease also highlights the adsorbent's effectiveness in dye sequestration, especially under conditions of elevated initial ion concentrations.

Experimentally, CR displayed the highest entropy value (382.2 mg g^{-1} at 298 K), while CV recorded a comparatively lower value of 333.8 mg g^{-1} (Fig. 9b). These equilibrium results are consistent with the predicted half-saturation concentrations of Zeo/AC, further confirming that as adsorption advances, the number of available binding sites becomes increasingly limited.[72,75]

3.2.8.2. Internal energy and free enthalpy. The internal energy (E_{int}) and free enthalpy (G) associated with the adsorption of CR and CV onto Zeo/AC were assessed using eqn (10). These calculations incorporated adsorption parameters, including the ion concentration at half-saturation ($C_{0.5}$), translation partition function (Z_v), occupied adsorption site density (N_m), and the number of ions per site (n). The results indicated that the free enthalpy values (G) were consistently negative at (eqn (11)), demonstrating that the adsorption process is both spontaneous and exothermic[74] (Fig. 9c and d).

Notably, G of CR values decreased as temperature increased, as illustrated in (Fig. 9c). The enthalpy decreases with increasing dye concentration for both CR and CV. This suggests that the adsorption process becomes more exothermic as more dye is adsorbed likely due to stronger interactions at higher coverage or cooperative adsorption effect. Furthermore, the negative free enthalpy (G) values confirm that the adsorption is thermodynamically favourable across all studied temperatures. Similarly, the internal energy (E_{int}) values were also negative and displayed a progressive reduction as temperature increased[72,74,75] (Fig. 9d).

Eint energy becomes more negative with increasing equilibrium concentration for both CR and CV which reflects a more energetically favorable adsorption process as more dye molecules interact with the adsorbent. The continuous drop suggests that the adsorbent (Zeo/AC) maintains high affinity for dye molecules even at higher concentrations, possibly due to a combination of surface heterogeneity and multiple interaction mechanisms (*e.g.*, π–π stacking, electrostatics).

The spontaneous nature of adsorption suggests that no external energy input is required, making Zeo/AC a cost-effective and efficient adsorbent for industrial applications.

3.3 Adsorption mechanisms and surface interactions

The comprehensive characterization and optimization studies provide insights into the complex adsorption mechanisms governing Congo red and crystal violet removal by the Zeo/AC nanocomposite, as illustrated in Fig. 10. The adsorption process involves multiple synergistic mechanisms that operate simultaneously, explaining the exceptional performance for both cationic and anionic dyes.

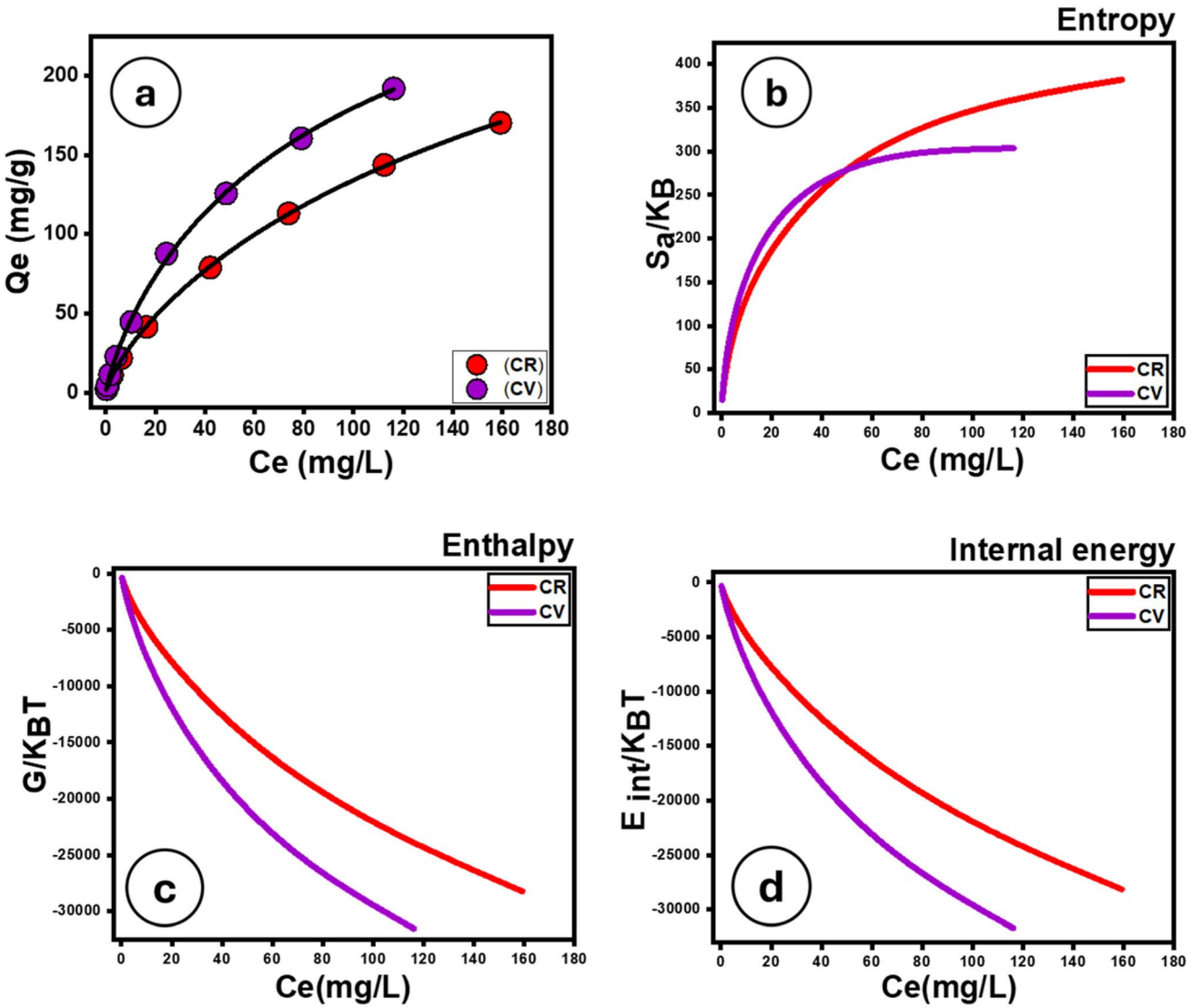

Fig. 9 Fitting of the advanced Monolayer model of one energy site at 298 K(a), and changes in entropy at 298 K (b), enthalpy at 298 K (c), and internal energy at 298 K (d).

3.3.1. Electrostatic interactions and ion exchange. Despite the unfavorable electrostatic conditions for Congo red adsorption at pH 7 (both adsorbent and dye negatively charged), significant removal efficiency was achieved. This suggests that electrostatic interactions, while important for crystal violet, are not the dominant mechanism for Congo red removal. For crystal violet, the favorable electrostatic attraction between the cationic dye (CV^+) and negatively charged adsorbent surface at pH 7 contributes significantly to the high adsorption capacity. The zeolite component provides specific ion exchange sites that can accommodate anionic species through localized charge compensation mechanisms, as demonstrated by recent mechanistic studies on anionic dye adsorption.[76–78]

3.3.2. π–π Stacking and hydrophobic interactions. Both Congo red and crystal violet possess extensive aromatic ring systems that can interact with the graphitic carbon structures in activated carbon through π–π stacking. These interactions are particularly strong for crystal violet due to its triphenylmethane structure containing three aromatic rings, while Congo red's multiple aromatic rings also engage in substantial π–π interactions. The enhanced performance compared to individual components suggests that the zeolite framework may orient dye molecules in configurations that optimize π–π interactions with carbon surfaces. This cooperative effect represents a key advantage of the composite approach and has been theoretically validated by molecular dynamics simulations conducted by Rassoulinejad-Mousavi *et al.* (2019) and Salahshoori *et al.* (2024).[79,80]

3.3.3. Hydrogen bonding and van der Waals forces. The abundant hydroxyl and amino groups in both dyes can form hydrogen bonds with surface functional groups on both zeolite and activated carbon components.[81,82] FTIR analysis revealed shifts in O–H and N–H stretching frequencies upon dye adsorption, confirming hydrogen bonding contributions.

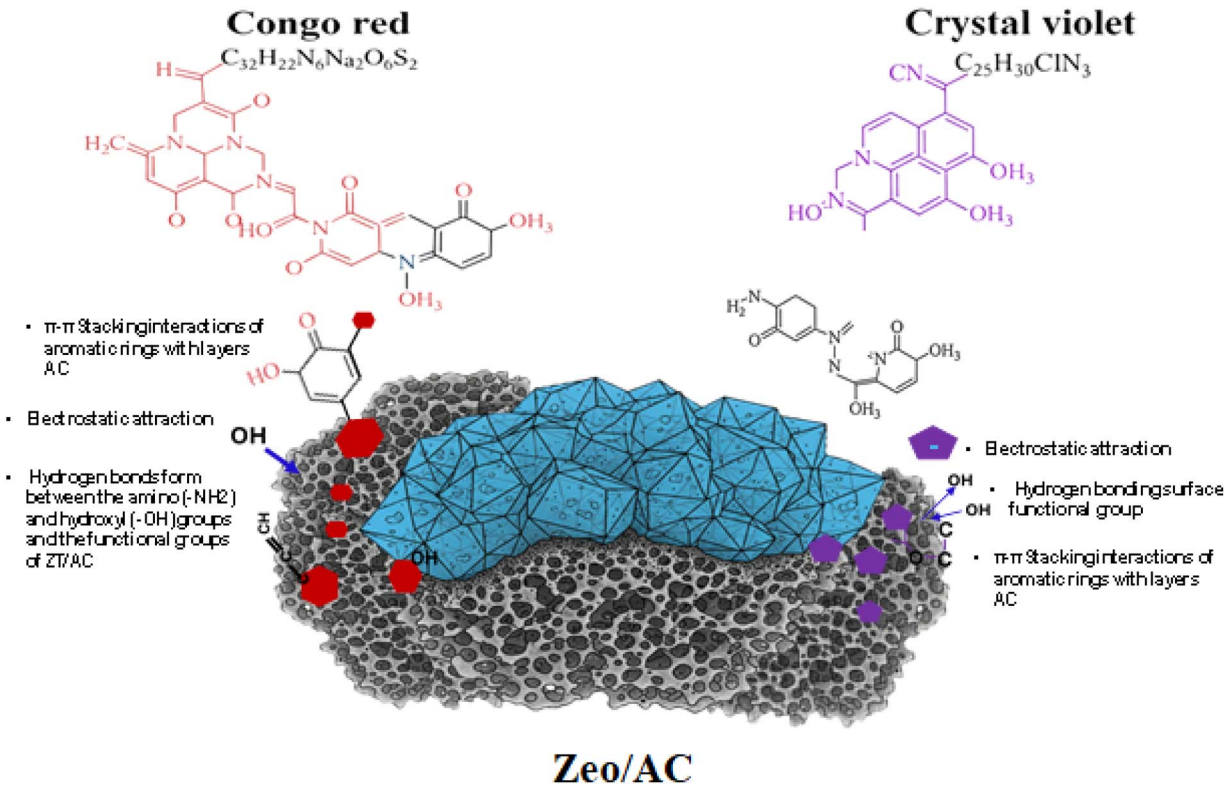

Fig. 10 Schematic diagram of adsorption mechanisms of Congo red and crystal violet onto Zeo/AC composite.

Additionally, van der Waals forces provide significant attractive interactions in the confined spaces of micropores, where the cumulative effect of multiple weak interactions contributes substantially to the overall binding energy, as described in theoretical work by Chabal *et al.* (2013).[83]

3.3.4. Pore filling and molecular sieving effects. The hierarchical pore structure of the Zeo/AC composite enables selective adsorption based on molecular size compatibility. Congo red (molecular dimensions: 2.6 × 1.0 × 0.4 nm) primarily accesses the mesopores of activated carbon, while crystal violet (molecular dimensions: 1.4 × 1.2 × 0.5 nm) can penetrate both zeolite micropores and carbon mesopores. This size complementarity between dye molecules and available pore spaces contributes to the selective adsorption behavior and high capacity observed for both dyes. This size-selectivity mechanism has been extensively studied by computational modeling approaches described by Chen *et al.* (2025) for hierarchical porous materials.[84]

3.3.5. Synergistic mechanism and cooperative effects. The integration of zeolite and activated carbon creates a unique synergistic system where multiple mechanisms operate cooperatively. The zeolite component provides ion exchange capacity and molecular sieving functionality, while activated carbon contributes high surface area and strong π–π interactions. This complementary action allows for efficient removal of both dyes through different dominant pathways: electrostatic attraction and pore filling for crystal violet, *versus* π–π stacking, hydrogen bonding, and ion exchange for Congo red. This multi-mechanistic approach explains the superior performance of the Zeo/AC nanocomposite in simultaneous dye removal applications.

3.4 Regeneration and reusability study

The regeneration performance of Zeo/AC nanocomposite was assessed using four regenerants including 0.1 M HCl, 0.1 M NaOH, 50% ethanol, and 0.1 M NaCl, as referred to (Fig. 11) Desorption efficiencies for Congo red (CR) were highest with NaOH (91.2%), followed by HCl (86.5%), ethanol (79.8%), and NaCl (61.4%). In contrast, Crystal violet (CV) showed maximum desorption with HCl (88.6%), then ethanol (81.2%), NaOH (77.9%), and NaCl (55.8%). Following desorption, the adsorbent was reused for five adsorption–desorption cycles under optimized conditions (pH 7, 55 °C, 60 min). The regeneration efficiencies over five cycles showed gradual decline, with HCl-treated samples retaining up to 82% capacity for CV and NaOH-treated samples retaining 76% capacity for CR by the fifth cycle. Other regenerants, particularly NaCl and ethanol, resulted in lower retention efficiencies, dropping below 70% after five cycles. These results indicate that 0.1 M HCl is the most suitable universal regenerant, particularly for maintaining performance in CV removal, while 0.1 M NaOH is effective for CR, though occasional acid rinsing may be required to prevent pore blockage and maintain long-term adsorbent integrity.

3.5 Cost analysis of the adsorption process

The economic feasibility of an adsorbent represents a critical determinant for its practical implementation in wastewater

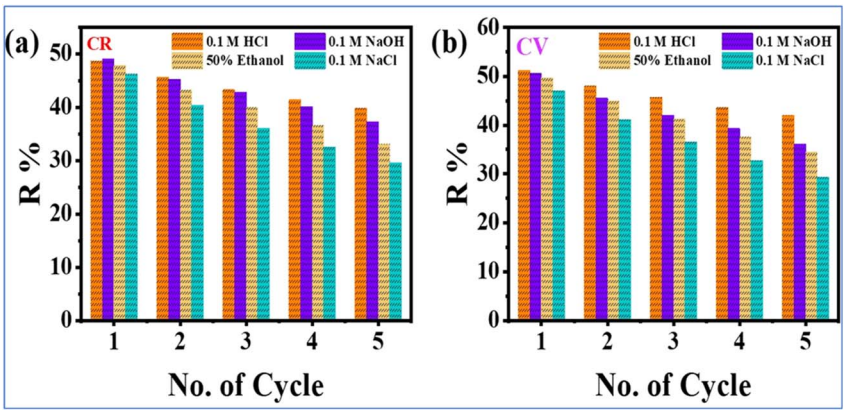

Fig. 11 Regeneration and reusability performance of zeolite/activated carbon nanocomposite over five adsorption–desorption cycles. Removal efficiency (R%) for (a) Congo Red (CR) and (b) Crystal Violet (CV) using different regenerants: 0.1 M HCl, 0.1 M NaOH, 50% ethanol, and 0.1 M NaCl. HCl shows the best overall regeneration performance for CV after five cycles, while NaOH is most effective for CR regeneration after five cycles.

Table 6 Cost analysis of the synthesized composite material

Material	Purchased quantity (g)	Total purchase cost (USD)	Purchasing cost (USD g^{-1})	Used quantity (g or mL)	Cost of used quantity (USD)
Zeolite	1 kg	12.89	0.0129	100	1.289
Activated carbon	Max. power (kW)	Unit cost of power	Cost		5.245
Equipment	1	0.15	0.3		
	1	0.19	4.56		
	1	0.24	0.24		
	1	0.21	2.52		
Milling autoclave	Total yield cost = 14.154	Total yield cost			
stirrer drying	USD For **153.89 g**	0.092 USD g^{-1}			

remediation applications. A comprehensive cost analysis must account for both energy requirements and chemical consumption during material synthesis. As detailed in Table 6, the production cost for 1.0 g of Zeo/AC composite material is calculated at approximately $0.092. Comparative evaluation with existing adsorbents (Table 7) reveals that the Zeo/AC composite demonstrates significantly enhanced cost-effectiveness relative to conventional water treatment materials reported in prior research. This favorable economic profile, coupled with its adsorption performance, positions the composite as a promising candidate for large-scale water purification applications.

3.6 Sustainability *via* a urea fuel cell

3.6.1. Effects of different scan rates and different urea concentrations on electrochemical oxidation. Cyclic voltammetry was utilized to examine the scan rate-dependent electrochemical response, applying the potential sweep technique over a potential range of 0.0 V to 1.00 V (Fig. 12a and b). Shows how the urea concentration affects the anode current density and electrocatalytic activity using the prepared material before and after adsorption. The findings indicate that adjusting the urea concentration has a pronounced impact on fuel cell efficiency. The study evaluated cyclic voltammetry (CV) current density at a scan rate of 100 mV s^{-1} with urea concentrations ranging from 0.10 M to 0.50 M. Experimental findings indicated a direct dependency of peak current density on urea concentration during electrooxidation, albeit with observed limitations. The scan rate was incrementally adjusted between 20 and 100 mV s^{-1} in an 1.00 M KOH electrolyte, as illustrated in (Fig. 12c and d). These data show that increasing the scan rate from 20 to 100 mV s^{-1} enhances the current density for both Zeo/AC before and after adsorption. This tendency can be attributed to more electroactive species reaching the electrode surface as the scan rate increased, which produced an increase in the current density.

An inverse correlation exists between urea concentration and oxidation peak current density in the case of the waste adsorbent, where higher urea levels result in lower current densities. This phenomenon is linked to the build-up of urea oxidation intermediates on the electrocatalyst surface, which progressively occupies active sites and induces catalyst poisoning. Due

Table 7 Comparative cost analysis of the synthesized Zeo/AC adsorbent with reported values in the literature

Material used	Cost (USD g^{-1})	unit	Reference
Zn–Fe LDH/PANI	12.48	USD g^{-1}	77
Activated carbon	1.33	USD kg^{-1}	78
LDH/PU/O-Pom	0.927	USD g^{-1}	79
Titania/graphene oxide	0.1875	USD g^{-1}	80
Zeo/AC	0.092	USD g^{-1}	This work

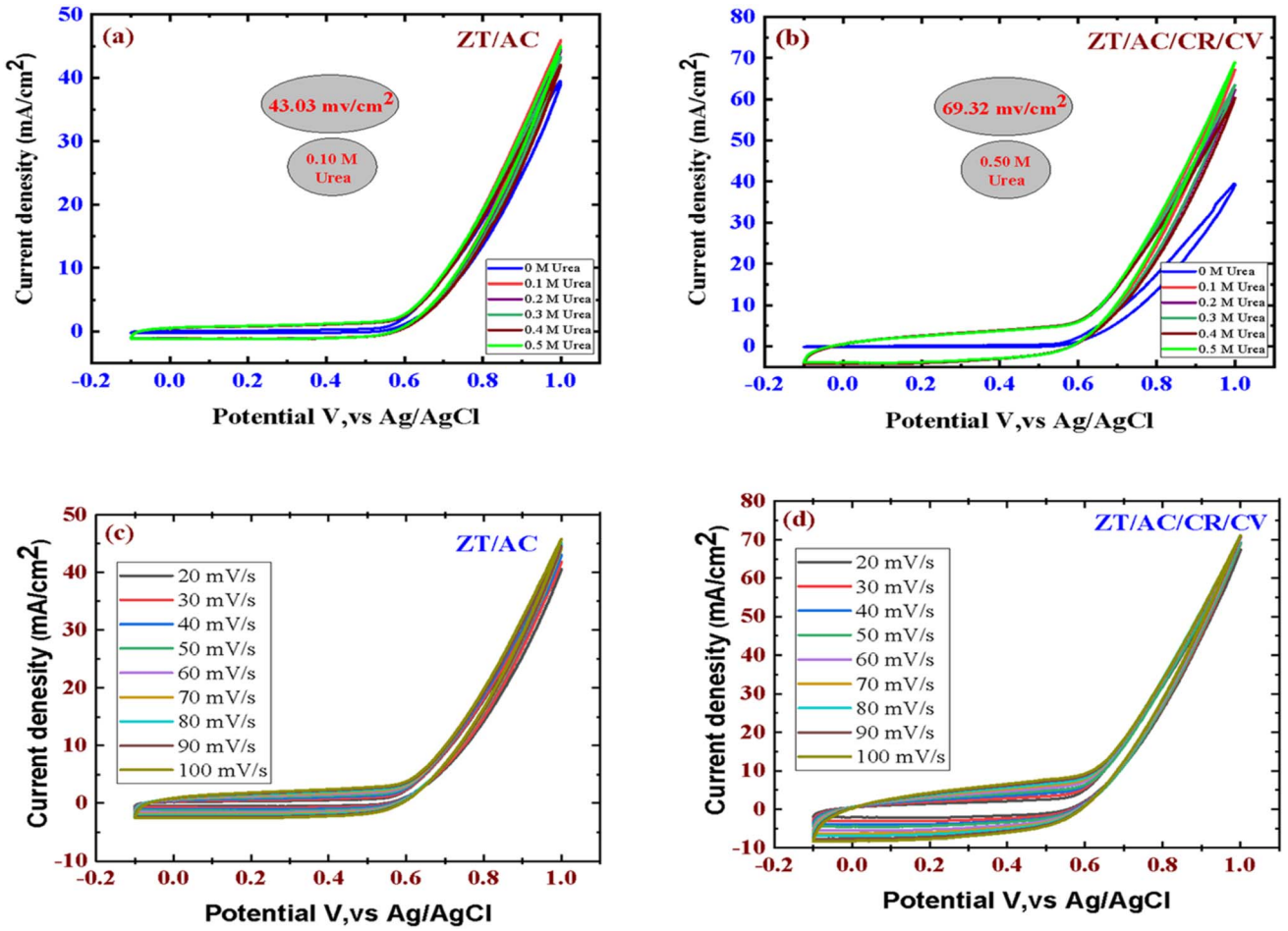

Fig. 12 (CV) curves for (a) Zeo/AC before and (b) Zeo/AC/CR/CV after electrochemical testing in 1 M NaOH, are displayed at a fixed scan rate of 100 mV s^{-1} with varying urea concentrations; (c and d) the effect of scan rates ranging from 20 to 100 mV s^{-1} within a potential window of 0–1.00 V.

to restricted diffusion of reactant species, the interaction with the electrocatalyst is hindered, causing a noticeable decrease in anodic peak current density.[85]

3.7 Greenness chemistry

Sustainable and environmentally friendly chemical processes, utilizing renewable resources, and making non-toxic and biodegradable products are all tenets of green chemistry. Implementing green chemical methods has many potential economic, environmental, and health benefits.

Green assessment tool, AGREEprep, evaluates the greenness of a sample preparation procedures.[85] The aspects of a sample preparation include the sample preparation site, safety of solvents, sustainability of materials, waste minimization, integration and automation of steps, reduction of sample volume, maximization of sample throughput, reduction of energy consumption, selection of environmentally friendly configurations for sample post-preparation, and operator safety. Shows the pictogram of AGREEprep. The final score and pictogram of AGREEprep GAC metric tool for our method is calculated (0.65) based on the evaluation of all 10 GSP principles (Fig. 13a).

MoGAPI method[71] quantifies and assesses the environmental impact of a method. Analytical processes, such as sample preparation, volume, health risks associated with solvents and reagents, instrumentation, waste quantity, handling, and so forth can be evaluated using MoGAPI method. Green indicates minimal environmental impact, whereas yellow and red indicate medium and heavy environmental impact, respectively. The MoGAPI program combines the accurate overall score with the benefits of GAPI's visual effect (Fig. 13b).

ComplexGAPI, complex green analytical procedure index, an easy tool that complements the existing GAPI metric, was proposed.[86] One hexagonal field was added to the original GAPI graph and it reflects the processes performed prior to the sample preparation step and final analysis. The generated ComplexGAPI pictogram for our analytical method is shown (Fig. 13c).

3.8 Implications for practical applications

The optimized conditions identified in this study (pH 7, 0.1 g/50 mL dosage, 55 °C, 60 min contact time) represent practically feasible parameters for industrial wastewater treatment

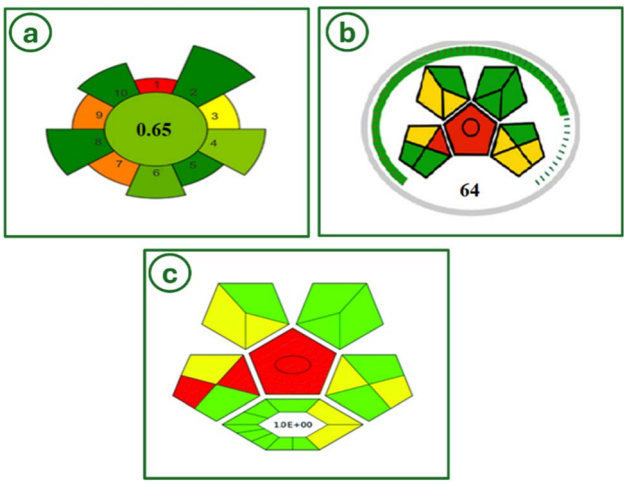

Fig. 13 The AGREEprep greenness tool (a), the MoGAPI greenness tool (b), and the ComplexGAPI greenness tool (c).

applications. The near-neutral pH eliminates the need for extensive pH adjustment, while the moderate temperature and short contact time ensure energy efficiency. These operational parameters align with industry standards for cost-effective water treatment processes, as outlined in recent techno-economic analyses by Elizondo-Noriega *et al.* (2020).[87]

The rapid kinetics and high removal efficiency make the Zeo/AC composite suitable for both batch and continuous flow applications. The dual functionality proposed for subsequent fuel cell applications adds significant value to the treatment process, transforming waste materials into energy storage components. This integrated approach to waste treatment and energy generation represents an emerging paradigm in sustainable technology development, as discussed by Guo *et al.* (2019).[88] The comprehensive understanding of adsorption mechanisms provides a foundation for process optimization and scale-up considerations. The multi-mechanism nature of the adsorption process ensures robust performance across varying operational conditions, addressing a key requirement for practical wastewater treatment systems. Scale-up methodologies for composite adsorbent systems have been detailed in recent engineering studies by Juela *et al.* 2022.[87]

Future research directions should focus on long-term stability assessment, and validation with real industrial effluents containing complex dye mixtures and interfering substances. The integration with fuel cell applications presents an innovative approach to sustainable water treatment with energy recovery potential, representing a promising avenue for circular economy implementation in water treatment technologies.[89]

4 Conclusion

This study successfully developed a novel zeolite-activated carbon nanocomposite for the efficient removal of both anionic and cationic dyes from aqueous solutions. The composite demonstrated exceptional adsorption performance, achieving high removal capacities for both dye types under neutral pH conditions, with rapid adsorption kinetics reaching equilibrium in a short timeframe. The adsorption process was found to follow chemisorption-based kinetics and involved multiple synergistic mechanisms including electrostatic interactions, π–π stacking, hydrogen bonding, and pore filling.

Thermodynamic analysis revealed that the adsorption process was spontaneous and predominantly governed by physical interactions. The composite exhibited excellent regeneration capability, maintaining high efficiency over multiple adsorption–desorption cycles. A significant innovation of this research lies in the successful demonstration of a circular economy approach, where the spent adsorbent was effectively repurposed for energy-related applications.

The integration of effective dye removal with subsequent resource recovery, combined with environmentally friendly synthesis methods, establishes this nanocomposite as a promising dual-function material for sustainable wastewater treatment and valorization applications.

Ethics approval and consent to participate

Not applicable, as the study did not apply to human or animal studies. The article does not include any studies on human participants or animals conducted by any of the authors.

Conflicts of interest

All authors declare that they have no conflicts of interest to disclose.

Data availability

The authors declare that the data supporting the findings of this study are available within the article.

Consent for publication: the authors confirm: this work represents original research that has not been previously published in any form; this manuscript has not been submitted for review or publication consideration elsewhere; the publication has received approval from all co-authors.

Supplementary information is available. See DOI: **https://doi.org/10.1039/d5ra06559c**.

Acknowledgements

This work was supported and funded by the Deanship of Scientific Research at Imam Mohammad Ibn Saud Islamic University (IMSIU) (grant number IMSIU-DDRSP2501).

References

1 Z. Qie, X. Lu, Z. Wang, D. Yang, Z. Liu, H. Xiang, H. Alhassawi and Z. Feng, Transformation in ring topology of Beta zeolite induced by chelation: Implications for CO2 and toluene adsorption under humid conditions, *Sep. Purif. Technol.*, 2025, 134677.

2 M. Hernández-Zamora, F. Martínez-Jerónimo, E. Cristiani-Urbina and R. O. Cañizares-Villanueva, Congo red dye affects survival and reproduction in the cladoceran Ceriodaphnia dubia. Effects of direct and dietary exposure, *Ecotoxicology*, 2016, **25**, 1832–1840.

3 P. O. Oladoye, M. O. Bamigboye, O. D. Ogunbiyi and M. T. Akano, Toxicity and decontamination strategies of Congo red dye, *Groundw. Sustain. Dev.*, 2022, **19**, 100844.

4 K. Z. Elwakeel, A. M. Elgarahy, G. A. Elshoubaky and S. H. Mohammad, Microwave assist sorption of crystal violet and Congo red dyes onto amphoteric sorbent based on upcycled Sepia shells, *J. Environ. Health Sci. Eng.*, 2020, **18**, 35–50.

5 Y. Tian, K. Wu, S. Lin, M. Shi, Y. Liu, X. Su and R. Islam, Biodegradation and decolorization of Crystal Violet dye by cocultivation with fungi and bacteria, *ACS Omega*, 2024, **9**, 7668–7678.

6 S. A. Elmelegy, M. S. Khalil and M. Saleh, Efficient biodegradation and detoxification of congo red *via* newly isolated Bacillus strains, Egypt, *J. Chem.*, 2024, **67**, 67–76.

7 M. Said, W. T. Rizki, W. R. Asri, D. Desnelli, A. Rachmat and P. L. Hariani, SnO2–Fe3O4 nanocomposites for the photodegradation of the Congo red dye, *Heliyon*, 2022, **8**, e09204.

8 E. S. Al-Farraj and E. A. Abdelrahman, Efficient photocatalytic degradation of congo red dye using facilely synthesized and characterized MgAl2O4 nanoparticles, *ACS Omega*, 2024, **9**, 4870–4880.

9 S. Mani and R. N. Bharagava, Exposure to crystal violet, its toxic, genotoxic and carcinogenic effects on environment and its degradation and detoxification for environmental safety, *Rev. Environ. Contam. Toxicol.*, 2016, **237**, 71–104.

10 S. Chakraborty, S. Chowdhury and P. Das Saha, Biosorption of hazardous textile dyes from aqueous solutions by hen feathers: Batch and column studies, *Korean J. Chem. Eng.*, 2012, **29**, 1567–1576.

11 H. K. Ho, M. Tripathi, S. Shukla, R. Singh, S. Singh, P. K. P. Singh, P. K. P. Singh, A. K. Shukla, S. Maurya, S. Pathak and V. K. Chaudhary, Physicochemical Investigations of Textile Wastewater and Process Parameter Optimization for Biodecolorization of Congo Red Dye by Pseudomonas aeruginosa MT-2 Strain, *J. Pure Appl. Microbiol.*, 2024, **18**(4), 2558–2569.

12 D. Bhatia, N. R. Sharma, J. Singh and R. S. Kanwar, Biological methods for textile dye removal from wastewater: A review, *Crit. Rev. Environ. Sci. Technol.*, 2017, **47**, 1836–1876.

13 B. Kamenická and G. Kuchtová, Critical review on electrooxidation and chemical reduction of azo dyes: economic approach, *Chemosphere*, 2024, **363**, 142799.

14 T. Setyaningtyas, K. Riyani, S. N. Handayani, and C. Firdharini, Degradation of Congo Red in batik wastewater using fenton reagent under visible rays, in *IOP Conf. Ser. Mater. Sci. Eng.*, IOP Publishing, 2019, 12027.

15 S. K. S. Masalvad and P. K. Sakare, Application of photo Fenton process for treatment of textile Congo-red dye solution, *Mater. Today: Proc.*, 2021, **46**, 5291–5297.

16 T. Linda, S. Muthupoongodi, X. S. Shajan and S. Balakumar, Photocatalytic degradation of congo red and crystal violet dyes on cellulose/PVC/ZnO composites under UV light irradiation, *Mater. Today: Proc.*, 2016, **3**, 2035–2041.

17 R. El Brychy, M. M. Rguiti, N. Rhazzane, M. D. Mellaoui, K. Abbiche, M. Abali, L. Bazzi, M. Hilali, S. El Issami and K. Groenen-Serrano, Electrochemical degradation of crystal violet using Ti/Pt/SnO2 electrode, *Appl. Sci.*, 2021, **11**, 8401.

18 M. N. Chollom, S. Rathilal, D. Alfa and V. L. Pillay, The applicability of nanofiltration for the treatment and reuse of textile reactive dye effluent, *Water*, 2015, **41**, 398–405.

19 D. Karisma, G. Febrianto, and D. Mangindaan, Removal of dyes from textile wastewater by using nanofiltration polyetherimide membrane, in *IOP Conf. Ser. Earth Environ. Sci.*, IOP Publishing, 2017, 12012.

20 E. Sahinkaya, S. Tuncman, I. Koc, A. R. Guner, S. Ciftci, A. Aygun and S. Sengul, Performance of a pilot-scale reverse osmosis process for water recovery from biologically-treated textile wastewater, *J. Environ. Manage.*, 2019, **249**, 109382.

21 A. Piotrowska-Kirschling, K. Szelągowska-Rudzka, J. Karczewski and J. Brzeska, Application of shrimp waste for the synthesis of polyurethane–chitosan materials with potential use in sorption of oil micro-spills in water treatment, *Sustainability*, 2021, **13**, 5098.

22 K. Nandal and R. Jindal, Enhanced dye adsorption *via* pectin/pullulan/kaolinite nanocomposite for wastewater treatment applications, *Int. J. Biol. Macromol.*, 2025, 145557.

23 A. Hamd, A. R. Dryaz, M. Shaban, H. AlMohamadi, K. A. Abu Al-Ola, N. K. Soliman and S. A. Ahmed, Fabrication and application of zeolite/acanthophora spicifera nanoporous composite for adsorption of congo red dye from wastewater, *Nanomaterials*, 2021, **11**, 2441.

24 R. Ullah, J. Sun, A. Gul, T. Munir and X. Wu, Evaluations of physico-chemical properties of TiO2/clinoptilolite synthesized *via* three methods on photocatalytic degradation of crystal violet, *Chin. J. Chem. Eng.*, 2021, **33**, 181–189.

25 E. Kweinor Tetteh and S. Rathilal, Adsorption and photocatalytic mineralization of bromophenol blue dye with TiO2 modified with clinoptilolite/activated carbon, *Catalysts*, 2020, **11**, 7.

26 R. Lafi, I. Montasser and A. Hafiane, Adsorption of congo red dye from aqueous solutions by prepared activated carbon with oxygen-containing functional groups and its regeneration, *Adsorpt. Sci. Technol.*, 2019, **37**, 160–181.

27 Y.-H. Wu, K. Xue, Q.-L. Ma, T. Ma, Y.-L. Ma, Y.-G. Sun and W.-X. Ji, Removal of hazardous crystal violet dye by low-cost P-type zeolite/carbon composite obtained from *in situ* conversion of coal gasification fine slag, *Microporous Mesoporous Mater.*, 2021, **312**, 110742.

28 S. Goswami, S. J. Phukan, G. Gupta, R. K. Pai, S. Rana, M. Roy, P. Kumar and S. Garai, Direct Urea Fuel Cells: A Review on Roadmap, Mechanism, Bottleneck, and Future Perspective, *Energy Fuels*, 2025, **39**, 6709–6727.

29 N. A. M. Barakat, O. M. Irfan, R. A. Almasri, A. M. K. Abdel-Aal and M. A. Ali, Enhanced performance of CoNi

nanoparticles-decorated activated carbon anode for direct urea fuel cells: from simulated solutions to real wastewater applications, *Chem. Eng. Commun.*, 2025, **212**, 1287–1301.
30 R. Ezzati, S. Ezzati and M. Azizi, Exact solution of the Langmuir rate equation: New Insights into pseudo-first-order and pseudo-second-order kinetics models for adsorption, *Vacuum*, 2024, **220**, 112790.
31 H. E. Reynel-Ávila, I. A. Aguayo-Villarreal, L. L. Diaz-Muñoz, J. Moreno-Pérez, F. J. Sánchez-Ruiz, C. K. Rojas-Mayorga, D. I. Mendoza-Castillo and A. Bonilla-Petriciolet, A review of the modeling of adsorption of organic and inorganic pollutants from water using artificial neural networks, *Adsorpt. Sci. Technol.*, 2022, **2022**, 9384871.
32 T. A. Saleh, Kinetic models and thermodynamics of adsorption processes: classification, in *Interface Sci. Technol.*, Elsevier, 2022, pp. 65–97.
33 S. P. D. M. Blanco, F. B. Scheufele, A. N. Módenes, F. R. Espinoza-Quiñones, P. Marin, A. D. Kroumov and C. E. Borba, Kinetic, equilibrium and thermodynamic phenomenological modeling of reactive dye adsorption onto polymeric adsorbent, *Chem. Eng. J.*, 2017, **307**, 466–475.
34 C. R. Girish, Determination of thermodynamic parameters in adsorption studies: a review, *Chem. Pap.*, 2025, 1–20.
35 W. Kamal, D. Essam, A. A. Allam, H. E. Alfassam, D. Abd El Tawab, S. A. Moaty and R. Mahmoud, Natural Egyptian zeolite ore as a novel layered adsorbent for petroleum wastewater treatment, *Chin. J. Anal. Chem.*, 2025, **53**, 100490.
36 A. R. Hidayu, N. F. Mohamad, S. Matali and A. Sharifah, Characterization of activated carbon prepared from oil palm empty fruit bunch using BET and FT-IR techniques, *Procedia Eng.*, 2013, **68**, 379–384.
37 O. A. Hussain, A. S. Hathout, Y. E. Abdel-Mobdy, M. M. Rashed, E. A. A. Rahim and A. S. M. Fouzy, Preparation and characterization of activated carbon from agricultural wastes and their ability to remove chlorpyrifos from water, *Toxicol. Rep.*, 2023, **10**, 146–154.
38 H. H. A. Claudel, O. R. Yves, D. Rolland, N. E. P. Salomon, T. C. Parfait, B. Florent and T. Theodore, Thermomechanical and physicochemical investigation of Raw clay bricks derived from Nomayo clay and palm shell powder lignocellulosic material, *Sci. Rep.*, 2025, **15**, 29540.
39 E. Hazem, M. A. Rafea, M. E. A. Zaki, M. A. Aborziza, M. A. Roshdy, M. M. Ismail, M. R. El-Aassar and F. M. Mohamed, Optimized adsorptive removal of organics from wastewaters using SAC-CNTs@ chitosan biogenic-composite: Modeling insight, *Int. J. Biol. Macromol.*, 2025, 146412.
40 M. A. Roshdy, M. A. Ataallah, A. I. Khedr, E. A. Mohamed, A. D. G. Al-Afify, M. H. Abdo, A. A. Othman and F. M. Mohamed, Spatial interpolation and isotherms studies for groundwater remediation utilizing Be/CNTs@ Alg nanocomposite material; case study: Beni-Suef aquifer floodplain, *Environ. Earth Sci.*, 2025, **84**, 365.
41 J. A. Laksmono, M. Sudibandriyo, A. H. Saputra and A. Haryono, Structured polyvinyl alcohol/zeolite/carbon composites prepared using supercritical fluid extraction techniques as adsorbent for bioethanol dehydration, *Int. J. Chem. Eng.*, 2019, **2019**, 6036479.
42 Z. Liu, X. Cheng, F. Muhammad and J. Zhang, Preparation of hierarchically porous zeolite templated carbon from fly ash with investigation into the adsorption behavior towards volatile organic compound, *J. Environ. Chem. Eng.*, 2024, **12**, 112254.
43 M. Rouhani, S. D. Ashrafi, K. Taghavi, M. N. Joubani and J. Jaafari, Evaluation of tetracycline removal by adsorption method using magnetic iron oxide nanoparticles (Fe3O4) and clinoptilolite from aqueous solutions, *J. Mol. Liq.*, 2022, **356**, 119040.
44 Y. Shi, W. Chen, S. Yang, C. Feng and X. Wang, Comparison of Two Types of Modified Zeolites and the Key Factors for Cd (II) Adsorption Processes in Micropolluted Irrigation Water, *Sustainability*, 2023, **15**, 10659.
45 C. Chen, K. Sun, C. Huang, M. Yang, M. Fan, A. Wang, G. Zhang, B. Li, J. Jiang and W. Xu, Investigation on the mechanism of structural reconstruction of biochars derived from lignin and cellulose during graphitization under high temperature, *Biochar*, 2023, **5**, 51.
46 Z. Li, D. Liu, Y. Cai, Y. Wang and J. Teng, Adsorption pore structure and its fractal characteristics of coals by N2 adsorption/desorption and FESEM image analyses, *Fuel*, 2019, **257**, 116031.
47 B. M. Ismail, A. M. Zayed, M. A. Roshdy, M. A. Rafea and F. M. Mohamed, Statistical modeling of mutagenic azo dye adsorption on bagasse activated carbon, *Sci. Rep.*, 2025, **15**, 20112.
48 K. Li, X. Li and B. Li, Investigation the adsorption behavior of functional carbon-based composites for efficient removing anions/cations in single and multicomponent systems, *Sep. Purif. Technol.*, 2022, **289**, 120737.
49 A. Kazempour and M. M. Bagheri-Mohagheghi, Activated carbon/zeolite hybrid nanocomposite for drinking water treatment applications: structural, optical, and surface adsorption properties, Water, Air, *Soil Pollut.*, 2023, **234**, 669.
50 A. Fernández-Andrade, B. Ávila-Toro, R. Baquerizo-Crespo, and J. M. Rodríguez-Díaz, Estimation of the bicomponent adsorption behavior of dyes: a modeling approach, in *Commun. Smart Technol. Innov. Soc. Proc. CITIS 2021*, Springer, 2021, pp. 41–51.
51 M. T. Nazari, C. Schnorr, C. V. T. Rigueto, I. Alessandretti, F. Melara, N. F. da Silva, L. Crestani, V. Ferrari, J. Vieillard and G. L. Dotto, A review of the main methods for composite adsorbents characterization, *Environ. Sci. Pollut. Res.*, 2022, **29**, 88488–88506.
52 M. Andrunik, M. Skalny, M. Gajewska, M. Marzec and T. Bajda, Comparison of pesticide adsorption efficiencies of zeolites and zeolite-carbon composites and their regeneration possibilities, *Heliyon*, 2023, **9**(10), e20572.
53 J. Mokrzycki, W. Franus, R. Panek, M. Sobczyk, P. Rusiniak, J. Szerement, R. Jarosz, L. Marcińska-Mazur, T. Bajda and M. Mierzwa-Hersztek, Zeolite composite materials from fly ash: An assessment of physicochemical and adsorption properties, *Materials*, 2023, **16**, 2142.

54 R. Panek, M. Medykowska, K. Szewczuk-Karpisz and M. Wiśniewska, Comparison of physicochemical properties of fly ash precursor, Na-P1 (C) zeolite–carbon composite and Na-P1 zeolite—adsorption affinity to divalent Pb and Zn cations, *Materials*, 2021, **14**, 3018.

55 T. D. Pham, T. T. Pham, M. N. Phan, T. M. V. Ngo, V. D. Dang and C. M. Vu, Adsorption characteristics of anionic surfactant onto laterite soil with differently charged surfaces and application for cationic dye removal, *J. Mol. Liq.*, 2020, **301**, 112456.

56 F. Parisi, Adsorption and separation of crystal violet, cerium (III) and lead (II) by means of a multi-step strategy based on k10-montmorillonite, *Minerals*, 2020, **10**, 466.

57 M. Ali Khan, R. Govindasamy, A. Ahmad, M. R. Siddiqui, S. A. Alshareef, A. A. H. Hakami and M. Rafatullah, Carbon based polymeric nanocomposites for dye adsorption: synthesis, characterization, and application, *Polymers*, 2021, **13**, 419.

58 J. Yu, A. Zou, W. He and B. Liu, Adsorption of mixed dye system with cetyltrimethylammonium bromide modified sepiolite: characterization, performance, kinetics and thermodynamics, *Water*, 2020, **12**, 981.

59 A. O. Adeleke, A. A. Al-Gheethi and Z. Daud, Optimization of operating parameters of novel composite adsorbent for organic pollutants removal from POME using response surface methodology, *Chemosphere*, 2017, **174**, 232–242.

60 O. Abdelwahab and W. M. Thabet, Natural zeolites and zeolite composites for heavy metal removal from contaminated water and their applications in aquaculture Systems: A review, *Egypt. J. Aquat. Res.*, 2023, **49**, 431–443.

61 M. Hasanzadeh, A. Simchi and H. S. Far, Nanoporous composites of activated carbon-metal organic frameworks for organic dye adsorption: Synthesis, adsorption mechanism and kinetics studies, *J. Ind. Eng. Chem.*, 2020, **81**, 405–414.

62 H. Alkhaldi, S. Alharthi, S. Alharthi, H. A. AlGhamdi, Y. M. AlZahrani, S. A. Mahmoud, L. G. Amin, N. H. Al-Shaalan, W. E. Boraie and M. S. Attia, Sustainable polymeric adsorbents for adsorption-based water remediation and pathogen deactivation: a review, *RSC Adv.*, 2024, **14**, 33143–33190.

63 Y. C. Wong, Y. S. Szeto, W. H. Cheung and G. McKay, Effect of temperature, particle size and percentage deacetylation on the adsorption of acid dyes on chitosan, *Adsorption*, 2008, **14**, 11–20.

64 H. Liu, C. Xu, X. Wei, Y. Ren, D. Tang, C. Zhang, R. Zhang, F. Li and C. Huo, 3D hierarchical porous activated carbon derived from bamboo and its application for textile dye removal: kinetics, isotherms, and thermodynamic studies, *Water, Air, Soil Pollut.*, 2020, **231**, 504.

65 H. Vijwani, M. N. Nadagouda, V. Namboodiri and S. M. Mukhopadhyay, Hierarchical hybrid carbon nano-structures as robust and reusable adsorbents: Kinetic studies with model dye compound, *Chem. Eng. J.*, 2015, **268**, 197–207.

66 J. Dai, J. Sun, A. Xie, J. He, C. Li and Y. Yan, Designed preparation of 3D hierarchically porous carbon material *via* solvothermal route and in situ activation for ultrahigh-efficiency dye removal: Adsorption isotherm, kinetics and thermodynamics characteristics, *RSC Adv.*, 2016, **6**, 3446–3457.

67 V. Durán-Egido, D. García-Giménez, J. C. Martínez-López, L. Pérez-Vidal and J. Carretero-González, Metal–organic frameworks as fillers in porous organic polymer-based hybrid materials: innovations in composition, processing, and applications, *Polymers*, 2025, **17**, 1941.

68 M. Mobarak, R. A. M. Ali and M. K. Seliem, Chitosan/activated coal composite as an effective adsorbent for Mn (VII): Modeling and interpretation of physicochemical parameters, *Int. J. Biol. Macromol.*, 2021, **186**, 750–758.

69 I. R. Sayed, A. M. Farhan, A. A. AlHammadi, M. I. El-Sayed, I. M. Abd El-Gaied, A. M. El-Sherbeeny, W. Al Zoubi, Y. G. Ko and M. R. Abukhadra, Synthesis of novel nanoporous zinc phosphate/hydroxyapatite nano-rods (ZPh/HPANRs) core/shell for enhanced adsorption of Ni2+ and Co2+ ions: Characterization and application, *J. Mol. Liq.*, 2022, **360**, 119527.

70 A. A. Ahmed-Anwar, M. A. Mohamed, A. A. Farghali, R. Mahmoud and M. E. M. Hassouna, Green UPLC method for estimation of ciprofloxacin, diclofenac sodium, and ibuprofen with application to pharmacokinetic study of human samples, *Sci. Rep.*, 2023, **13**, 17613.

71 H. M. Nassef, H. A. Ahmed, A. H. Bashal, M. A. El-Atawy, T. Y. A. Alanazi, S. M. Mahgoub and M. A. Mohamed, A novel Six Sigma approach and eco-friendly RP-HPLC technique for determination of pimavanserin and its degraded products: Application of Box–Behnken design, *Rev. Anal. Chem.*, 2024, **43**, 20230073.

72 F. Dhaouadi, L. Sellaoui, H. E. Reynel-Ávila, V. Landín-Sandoval, D. I. Mendoza-Castillo, J. E. Jaime-Leal, E. C. Lima, A. Bonilla-Petriciolet and A. Ben Lamine, Adsorption mechanism of Zn2+, Ni2+, Cd2+, and Cu2+ ions by carbon-based adsorbents: interpretation of the adsorption isotherms via physical modelling, *Environ. Sci. Pollut. Res.*, 2021, **28**, 30943–30954.

73 F. Dhaouadi, L. Sellaoui, M. Badawi, H. E. Reynel-Ávila, D. I. Mendoza-Castillo, J. E. Jaime-Leal, A. Bonilla-Petriciolet and A. Ben Lamine, Statistical physics interpretation of the adsorption mechanism of Pb2+, Cd2+ and Ni2+ on chicken feathers, *J. Mol. Liq.*, 2020, **319**, 114168.

74 L. Sellaoui, H. Guedidi, L. Reinert, S. Knani, L. Duclaux and A. Ben Lamine, Experimental and theoretical studies of adsorption of ibuprofen on raw and two chemically modified activated carbons: new physicochemical interpretations, *RSC Adv.*, 2016, **6**, 12363–12373.

75 K. Y. Foo and B. H. Hameed, Insights into the modeling of adsorption isotherm systems, *Chem. Eng. J.*, 2010, **156**, 2–10.

76 J. Ma, B. Cui, J. Dai and D. Li, Mechanism of adsorption of anionic dye from aqueous solutions onto organobentonite, *J. Hazard. Mater.*, 2011, **186**, 1758–1765.

77 A. M. Herrera-González, M. C. Reyes-Angeles and A. A. Peláez-Cid, Adsorption of anionic dyes using composites based on basic polyelectrolytes and physically activated carbon, *Desalin. Water Treat.*, 2021, **230**, 346–358.

78 W. Al-Gethami, M. A. Qamar, M. Shariq, A.-N. M. A. Alaghaz, A. Farhan, A. A. Areshi and M. H. Alnasir, Emerging environmentally friendly bio-based nanocomposites for the efficient removal of dyes and micropollutants from wastewater by adsorption: a comprehensive review, *RSC Adv.*, 2024, **14**, 2804–2834.

79 I. Salahshoori, Q. Wang, M. A. L. Nobre, A. H. Mohammadi, E. A. Dawi and H. A. Khonakdar, Molecular simulation-based insights into dye pollutant adsorption: a perspective review, *Adv. Colloid Interface Sci.*, 2024, **333**, 103281.

80 S. M. Rassoulinejad-Mousavi, J. Azamat, A. Khataee and Y. Zhang, Molecular dynamics simulation of water purification using zeolite MFI nanosheets, *Sep. Purif. Technol.*, 2020, **234**, 116080.

81 L. Zhang, J. Lu, Q. Liu, Y. Guo, L. Sun, R. Jiang and X. Song, An organic cage-based adsorbent for removing triphenylmethane dyes based on charge-assisted hydrogen bonding, *J. Environ. Chem. Eng.*, 2025, **13**, 116028.

82 R. Srivastava and D. C. Rupainwar, Removal of hazardous triphenylmethane dye through adsorption over waste material-mango bark powder, *Indian J. Chem. Technol.*, 2011, **18**, 469–474.

83 Y. Chabal, Spectroscopic studies of van der Waals bonding and interactions in microporous materials, in *APS March Meet*, Abstr., 2013, pp. F6–F7.

84 Y. Chen, Z. Qu, F. Sun, X. Li, J. Wang, J. Li, J. Gao and G. Zhao, Revealing the role of hierarchical pore in alleviating competitive adsorption between different-sized VOCs: A mechanistic study using coal-based activated carbon with tunable porous hierarchy, *Sep. Purif. Technol.*, 2025, **359**, 130609.

85 R. Baronia, J. Goel, J. Kaswan, A. Shukla, S. K. Singhal and S. P. Singh, PtCo/rGO nano-anode catalyst: enhanced power density with reduced methanol crossover in direct methanol fuel cell, *Mater. Renew. Sustain. Energy*, 2018, **7**, 27.

86 R. A. Sheldon, Metrics of green chemistry and sustainability: past, present, and future, *ACS Sustain. Chem. Eng.*, 2018, **6**, 32–48.

87 A. Elizondo-Noriega, N. Tiruvengadam, C. Fedler and M. Beruvides, Techno-Economic Analysis of Integrated Wastewater Treatment and Biomass Energy Generation Technologies: A Systematic Literature Review, *Conference: 2020 IISE Annual Conference*, 2020.

88 Z. Guo, Y. Sun, S.-Y. Pan and P.-C. Chiang, Integration of green energy and advanced energy-efficient technologies for municipal wastewater treatment plants, *Int. J. Environ. Res. Public Health*, 2019, **16**, 1282.

89 G. Mannina, H. Gulhan and B.-J. Ni, Water reuse from wastewater treatment: The transition towards circular economy in the water sector, *Bioresour. Technol.*, 2022, **363**, 127951.